

# On the resolution sensitivity of equatorial precipitation in a GFDL global atmospheric model

Pu Lin<sup>1</sup>, Yi Ming<sup>2,3</sup> and Thomas Robinson<sup>2</sup>

<sup>1</sup>Program in Atmospheric and Oceanic Sciences, Princeton University

<sup>2</sup>NOAA/OAR/Geophysical Fluid Dynamics Laboratory

<sup>3</sup>now at Schiller Institute for Integrated Science and Society, Boston College

## Key Points:

- Aquaplanet simulations are performed in a global atmospheric general circulation model at progressively finer resolution from 50km to 6km.
- The stronger resolved precipitation at finer resolution cannot be explained by changes in the vertical velocity amplitudes.
- The simulated tropical precipitation becomes more organized at the planetary scale in models with the finer resolution.

---

Corresponding author: Pu Lin, [pulin@princeton.edu](mailto:pulin@princeton.edu)

## Abstract

We performed a series of aquaplanet simulations at the horizontal resolution from 50km to 6km with identical parameterization settings using the Geophysical Fluid Dynamics Laboratory’s Atmosphere Model version 4 implemented with the two-moment Morrison-Gottelman cloud microphysics with prognostic precipitation (GFDL AM4-MG2). At the finer resolution, the global mean resolved-scale precipitation increases and that from cumulus parameterization decreases. The model also simulates less/thinner clouds over the low latitudes and more/thicker clouds over the high latitudes as the resolution increases. The precipitation over the deep tropics is investigated in detail. We find little resolution sensitivity in the daily mean precipitation extremes. Changes of the equatorial resolved precipitation with resolution cannot be fully explained by the resolution dependence in the vertical velocity amplitude. We report a robust sensitivity in the convective organization over the deep tropics to the model resolution. In simulations of finer resolution, the localized convection is suppressed, and the organized convective system associated with large-scale circulations becomes more prominent.

## Plain Language Summary

Convection and precipitation events are important components of the climate system, but they are often too small to be directly resolved by a typical climate model. Increasing the resolution is therefore desirable but does not automatically solve all the model biases. Here, we seek a more physical understanding of how the simulated climate by a climate model is affected by its horizontal resolution. We systematically increased the horizontal resolution in a global atmospheric model from 50km to 6km. The difference between the high and low resolution simulations is not only evident in the small scales, but also evident in the large scales as well. In particular, our model with finer resolution simulates a closer relationship between convection events and large-scale circulation.

## 1 Introduction

The advance of the general circulation models (GCMs) is accompanied by increasing resolutions. It has recently become computationally feasible to simulate the global atmospheric general circulation at a horizontal resolution of a few kilometers for extensive periods of time. This is the so-called convective “gray-zone” resolution at which convection, especially the deep one, starts to be explicitly resolved (e.g., Shin & Hong, 2015; Jeevanjee, 2017; Gao et al., 2017). This new generation of models is referred to as global storm resolving models (GSRMs), global cloud resolving models (GCRMs), or global convection-permitting models in the literature. They generally show notable improvements compared to the current generation of GCMs with a typical resolution of  $\sim 100\text{km}$ , especially with regards to precipitation and convection (e.g., Stevens et al., 2019; Satoh et al., 2019; Caldwell et al., 2021). However, considerable inter-model spread and model biases still exist among these GSRMs (Stephan et al., 2019; Heim et al., 2021; Judt et al., 2021; Roh et al., 2021; Lang et al., 2021), and there is no consensus regarding when to turn off cumulus parameterization or how to make the cumulus parameterization scale-aware at the gray-zone resolution (e.g., Gao et al., 2017; Arnold et al., 2020; Satoh et al., 2019). Sorting out this chaos requires a physical understanding of the model’s sensitivity to resolution.

Several studies have investigated the resolution sensitivity in GCMs, most of which pushes the horizontal resolution up to 25km or  $0.25^\circ$ . A common feature of the resolution sensitivity found in these GCM simulations is that the resolved precipitation increases with model resolution while the parameterized precipitation decreases (e.g., Wehner et al., 2014; Herrington & Reed, 2017; Terai et al., 2018; Herrington & Reed, 2020). The stronger mean resolved precipitation at the finer resolution is often manifested in an intensification of the precipitation extremes, and the stronger extremes persist when the

precipitations are coarse-grained and sampled at daily frequency (Li et al., 2011; Wehner et al., 2014; O’Brien et al., 2016; Rios-Berrios et al., 2020). Studies have attributed the stronger mean resolved precipitation and stronger precipitation extremes to the stronger amplitude of vertical velocity at the finer scales (Li et al., 2011; Rauscher et al., 2016; Herrington & Reed, 2017, 2020). The reduced parameterized precipitation is in response to changes in the background state due to the resolved processes (Herrington & Reed, 2020).

While the increase of vertical velocity magnitude with horizontal resolution is commonly observed in various model simulations and well established in theory (Jeevanjee, 2017, and references therein), there are several factors that may potentially counteract its effect on the resolved precipitation. Precipitation is expected to increase with precipitable water (e.g., Bretherton et al., 2004; Ahmed & Schumacher, 2015; Terai et al., 2018), but many models simulate a decrease in precipitable water with resolution at least for the global average (Williamson et al., 1995; Herrington & Reed, 2017; Terai et al., 2018). Mean and extreme precipitation are also affected by precipitation efficiency. Reduced precipitation efficiency with finer resolution is reported in cloud resolving models (Lutsko & Cronin, 2018; Jeevanjee & Zhou, 2022). Studies also found the precipitation extremes to be strongly affected by the degree of convective aggregation and organization (Bao et al., 2017; Pendergrass, 2020, and references therein). Simulations from idealized cloud resolving models under the radiative-convective equilibrium typically show that coarser resolution is favored for self-aggregation (Muller & Held, 2012; Muller & Bony, 2015), indicating a potential resolution dependence of precipitation via changes of convective organization. However, it is worth noting that these cloud resolving models are generally at the resolution of sub-kilometer or finer, and the resolution sensitivity found in those models may not extend to the lower resolution regime.

In addition to precipitation, previous studies also reported resolution sensitivity in Hadley cell strength (Williamson et al., 1995), location of the eddy driven jet (Lu et al., 2015), and switching from single to double intertropical convergence zone (ITCZ; Yu et al., 2014; Benedict et al., 2017; Retsch et al., 2019). But these results appear to be more model dependent.

Here, we start with a state-of-art atmospheric GCM, and systematically increase the horizontal resolution from a typical GCM value to a GSRM one. We perform aquaplanet simulations using a non-hydrostatic dynamical core and document the model behavior as it approaches the convective gray-zone. At higher resolutions than previous GCM studies, we find that some of the previously reported resolution sensitivities no longer hold and new resolution sensitivity emerges in our simulations. In the following, section 2 describes the model and the simulation design, section 3 presents the results and a summary and discussion are given in section 4.

## 2 Model description and experiment setup

We performed aquaplanet simulations using an updated version of the Geophysical Fluid Dynamics Laboratory (GFDL) Atmosphere Model version 4 (AM4) referred to as AM4-MG2 (Guo et al., 2021). AM4-MG2 is built upon GFDL’s most recent atmospheric model AM4.0 (Zhao et al., 2018a, 2018b), replacing the original Rotstayn-Klein microphysical scheme (Rotstayn, 1997; Jakob & Klein, 2000; Donner et al., 2011) with the more sophisticated MG2 scheme (Gettelman & Morrison, 2015). This two-moment bulk cloud microphysics scheme with prognostic precipitation improves simulations of coastal stratocumulus. AM4-MG2 also implements a new mineral dust and temperature-dependent ice nucleation scheme (Fan et al., 2019). Same as AM4.0, AM4-MG2 utilizes the GFDL finite-volume cubed-sphere dynamical core (FV3, Harris, Zhou, Chen, & Chen, 2020), a double-plume convection scheme (Zhao et al., 2018b), the Tiedtke scheme for cloud amount (Tiedtke, 1993), and the Lock scheme for planetary boundary layer (Lock

et al., 2000). Detailed configuration of AM4-MG2 and its performance are documented in Guo et al. (2021).

Different from the simulations presented by Zhao et al. (2018a) or Guo et al. (2021), we use the nonhydrostatic solver described by Harris, Chen, et al. (2020) instead of a hydrostatic one. Hydrostatic approximation starts to break down at the scale of a few kilometers and leads to large errors for sub-kilometer resolutions (Jeevanjee, 2017). While solutions from a hydrostatic solver may not differ much from those from a nonhydrostatic one for most of the resolutions considered here, we use the nonhydrostatic solver for all resolutions for consistency.

The model is run in aquaplanet configuration by prescribing a zonally symmetric sea surface temperature profile (“Control” in Neale & Hoskins, 2000), which is invariant in time. The aquaplanet simulations are widely used for evaluating the performance of the atmospheric models (e.g., Neale & Hoskins, 2000; Blackburn et al., 2013; Medeiros et al., 2015; Merlis & Held, 2019). Aquaplanet simulations using AM4.0 have been used to study tropical cyclones (G. Zhang et al., 2021) and have contributed to the Cloud Feedback Model Intercomparison Project (CFMIP) (Silvers et al., 2018). By using an idealized lower boundary, the aquaplanet simulations are simpler and therefore easier to understand than the more realistic simulations while preserving the general behavior of the more realistic models, especially for tropical phenomena such as the ITCZ, tropical cyclones and convectively coupled equatorial waves. But we note that the aquaplanet settings ignore any resolution sensitivity arising from resolving topography and surface conditions.

This is different from the simulations proposed in the DYNAmics of the Atmospheric general circulation Modeled On Non-hydrostatic Domains (DYAMOND) project and its successor DYAMOND2, which intends to compare GSRMs developed around the world under the real world settings with each other and against observations (Stevens et al., 2019). In particular, the GFDL System for High-resolution prediction on Earth-to-Local Domains (SHiELD, Zhou et al., 2019; Harris, Zhou, Lin, et al., 2020) is a participant of the DYAMOND project. SHiELD has been configured to run at different resolutions and its performance at a globally uniform 3km grid (X-SHiELD configuration) has been reported by F. Zhang et al. (2019) and Harris et al. (2023). The AM4-MG2 model used here shares the same dynamical core as SHiELD, but the physics packages in the two models are generally disparate. We hope that our idealized aquaplanet simulations at similar resolutions may help to understand the simulations by SHiELD and to interpret the inter-model differences and model biases seen in DYAMOND simulations (Heim et al., 2021; Judt et al., 2021; Roh et al., 2021; Lang et al., 2021).

We perform a series of simulations with varying horizontal resolutions. AM4 model grid has cubed-sphere topology and its horizontal resolution is denoted by the number of grid boxes along the side of each cubed face such that a resolution of  $Cn$  signifies  $n \times n$  grid boxes per cubed face. Simulations are done at the resolutions of C192, C384, C768 and C1536, corresponding to a nominal resolution of about 50km, 25km, 13km, and 6km, respectively. As listed in Table 1, both physical and dynamical time steps are reduced to accommodate the increased resolution. Note that the radiation time step is different from physical time step in this model, which does not change with resolution (3 hours for longwave and 1 hour for shortwave). The vertical resolution are kept identical for all these simulations. The model consists of 33 model levels with a model top at 1 hPa (see Open Research for specification). We use the fourth order divergence and vorticity damping with the same non-dimensional damping coefficients for all simulations here, which effectively yield weaker damping for higher resolution runs. A more detailed description regarding the diffusion settings can be found in the appendix. All the tuning parameters (including those used in cumulus parameterization) are kept identical for all the simulations considered here. The detailed configuration of each simulation is included in the Open Research section. We use the same parameters as Guo et al. (2021) for their his-



**Table 1.** Experiment setting

Experiment	$\Delta x$ (km)	$\Delta t$ phy (s)	$\Delta t$ dyn (s)
C192	50	1200	75
C384	25	600	28.6
C768	13	300	16.7
C1536	6	200	8.3

torical AMIP simulations at the resolution of C96(100km). For a fair comparison, the outputs from all experiments are remapped to the same  $0.5^\circ \times 0.5^\circ$  grid. The spatial remapping is done conservatively using `fregid` (<https://github.com/NOAA-GFDL/FRE-NCtools>). We use the coarse-grained data to evaluate the climatology, and evaluate variability using both coarse-grained and raw data.

The model is set to be on the perpetual equinox and run for one year. The first three months are considered as spin-up and discarded. Greenhouse gases concentrations are set to constant values ( $CO_2$ : 348 ppmv,  $CH_4$ : 1.65 ppmv,  $N_2O$ : 0.306 ppmv,  $CFC-11$ : 264.325 ppbv,  $CFC-12$ : 536 pptv,  $CFC-113$ : 82.765 pptv,  $HCFC-22$ : 13.455 pptv), and the solar constant is  $1365 \text{ W/m}^2$ . Aerosol emissions are set to the year 1860 level based on the CMIP6 forcing data (Eyring et al., 2016). Aerosol emissions include a seasonal cycle. We note that the simulated precipitation shows strong hemispherical symmetry and weak seasonal dependence despite the asymmetric and time-varying aerosol emissions.

### 3 Results

#### 3.1 Climatology

We start by calculating a few globally integrated indices representing the basic hydrological, radiative and dynamical climatology simulated in these experiments. Table 2 lists the global mean total precipitation rate (`PREC_tot`), precipitation at the resolved scale (`PREC_res`), precipitation from the deep plume in the cumulus parameterization (`PREC_deep`) and precipitation from the shallow plume (`PREC_shallow`). The global mean resolved precipitation increases with resolution. The parameterized precipitation, on the other hand, decreases with resolution, which mostly comes from the deep plume. This divergent response to resolution changes between the resolved and parameterized precipitation is consistent with previous studies (e.g., Wehner et al., 2014; Herrington & Reed, 2017; Terai et al., 2018; Herrington & Reed, 2020). Changes in the total precipitation with resolution is in general small and insignificant, but statistically significant reduction is found at the highest resolutions considered (from C768 to C1536), which hints at a regime shift.

The latitudinal distribution of the precipitation is plotted in Fig. 1. The parameterized precipitation from the deep plume shows consistent reduction with resolution at all latitudes, while changes in the shallow plume are less coherent across latitudes and generally weak. The latitudinal structure of the resolved precipitation changes is more complex. The resolved precipitation climatology shows a strong peak at the equator and a secondary peak centered around  $40^\circ$ . As the resolution increases, the mid-latitude peak becomes wider but little changes in the peak amplitude. The equatorial precipitation peak, on the other hand, responds to model resolution variations mainly via its amplitude but not the width. The equatorial resolved precipitation increases with resolution from C192 to C768, but decreases slightly from C768 to C1536. The total precipitation from both resolved and parameterized processes shows a similar two-peak structure as the resolved precipitation, but its variations across resolution is generally subtle.

Given these changes in precipitation as resolution varies, other components in the hydrological cycle are expected to vary with resolution as well. Herrington and Reed (2017) reported a drying atmosphere with resolution in terms of total precipitable water and cloud fraction. We see a similar reduction in the global mean precipitable water (measured by water vapor path WVP) and cloud fraction with resolution (Table 2). We further examined the clouds simulated in these experiments by evaluating the cloud liquid and ice water path (LWP, IWP) as well as the cloud radiative effect (CRE). Most liquid water resides in the low cloud and exerts its radiative effects in the shortwave bands, while ice water mostly resides in the high clouds and has stronger effects in the longwave bands. As shown in Fig. 1, finer resolution runs show less cloud water and weaker CRE over regions equatorward of  $\sim 35^\circ$ , but more cloud water and stronger CRE on the poleward side. This compensation between the lower and higher latitudes is more substantial for the ice phase and the longwave CRE, which show appreciable resolution dependence locally (Figs. 1e, h) but trivial changes in the global mean (Table 2). The LWP and shortwave CRE, on the other hand, is dominated by changes over the subtropics. A reduction of  $12 \text{ W/m}^2$  in the global mean shortwave CRE is seen from C192 to C1536. Table 2 also list the global mean outgoing longwave radiation (OLR) and upward shortwave radiation at the top of the atmosphere (SWUP TOA). Changes in these all-sky radiative flux are largely driven by changes in clouds, whereas the variation in the global mean clear-sky radiative flux across resolutions does not exceed  $0.5 \text{ W/m}^2$  (not shown).

We also evaluate the general circulation simulated in these simulations. Following Lu et al. (2015), we diagnose the intensity of the extratropical eddy-driven jet by the maximum zonal mean zonal wind speed at 250 hPa ( $U_{\text{max}250}$ ) and the location of the jet by the latitude of where the maximum zonal mean zonal wind occurs at 850 hPa ( $\phi_{\text{umax}850}$ ). Lu et al. (2015) reported that the extratropical jet tends to be weaker but more poleward as the resolution increases, but converges for resolutions finer than 50km. Here, we find no monotonic relationship between the jet intensity or location with the resolution, which are all at or finer than 50km. The Hadley cell is diagnosed using the zonal mean mass flux stream function at 500 hPa following Lu et al. (2007). We find that neither the intensity nor the width of the Hadley cell shows any strong or robust sensitivity to the resolution changes considered here.

In short, we find a similar resolution dependence in the globally averaged precipitation and other hydrometeors as reported in earlier GCM studies, that is, an increase in the resolved precipitation with resolution and a decrease in the parameterized precipitation, total precipitable water and cloud fraction. However, we find that changes in these hydrometeors are not uniform across latitudes and several cloud-related variables show opposite sensitivity between low and high latitudes. In addition, we note that our model simulates a larger cloud fraction and a smaller global mean precipitation than earlier aquaplanet simulations (Williamson et al., 2012, 2013), which may not only arise from differences in model resolution but also from differences in model physics. We defer discussions on such inter-model difference in climatology to a future study. In the following subsections, we will provide a thorough investigation on the resolution dependence of the equatorial precipitation.

### 3.2 Precipitation intensity distribution in the deep tropics

In this subsection, we focus on the resolved precipitation in the deep tropics. This is the region where the strongest precipitation and deepest convection occur. Results of this subsection are based on one month of data (the 6th month) and are insensitive to the choice of the month. We analyze data on the lat-lon grid between  $5.5^\circ\text{N}$  and  $5.5^\circ\text{S}$ . For data on the native model grid, we analyze a swath of grids centered at the equator, that is  $24 \times 768$  grids in C192,  $48 \times 1536$  grids in C384,  $96 \times 3072$  grids in C768 and  $192 \times 6144$  grids in C1536. These grids roughly correspond to a latitude band between  $5.56^\circ\text{N}$ - $5.56^\circ\text{S}$  covering all longitudes. Note that the area of each native model grid and

**Table 2.** Summary of mean climate diagnostics. Bold font indicates the difference against its immediate lower resolution counterpart is statistically significant, based on the Student's *t* test of monthly data at 95% confidence level. Orange color indicates a positive difference and blue color indicates a negative difference. The statistics are evaluated using monthly mean data. See text for the definitions of the variables.

	C192	C384	C768	C1536
PREC_tot (mm/day)	2.56	<b>2.59</b>	<b>2.58</b>	<b>2.52</b>
PREC_res (mm/day)	1.81	<b>2.00</b>	<b>2.20</b>	<b>2.22</b>
PREC_deep (mm/day)	0.42	<b>0.26</b>	<b>0.07</b>	<b>0.02</b>
PREC_shallow (mm/day)	0.33	0.33	<b>0.32</b>	<b>0.28</b>
OLR ( $W/m^2$ )	211.73	212.64	<b>213.63</b>	<b>212.55</b>
SWUP TOA ( $W/m^2$ )	115.86	<b>114.12</b>	<b>108.74</b>	<b>103.44</b>
Longwave CRE ( $W/m^2$ )	43.66	43.12	<b>42.29</b>	<b>43.07</b>
Shortwave CRE ( $W/m^2$ )	-79.74	-78.15	<b>-73.00</b>	<b>-67.80</b>
WVP ( $kg/m^2$ )	20.76	<b>20.45</b>	<b>20.07</b>	20.02
LWP ( $g/m^2$ )	72.08	<b>69.92</b>	<b>65.59</b>	<b>59.97</b>
IWP ( $g/m^2$ )	63.52	63.04	61.12	61.44
cloud fraction (%)	80.49	<b>79.1</b>	<b>76.09</b>	<b>73.89</b>
Umax250 ( $m/s$ )	47.96	<b>44.96</b>	<b>47.41</b>	48.33
$\phi_{umax850}$	39.49°	<b>41.94°</b>	<b>41.97°</b>	42.55°
Hadley cell strength ( $10^{11} kg/s$ )	1.58	1.64	1.64	1.59
Hadley cell edge	27.06°	<b>27.79°</b>	27.88°	27.75°

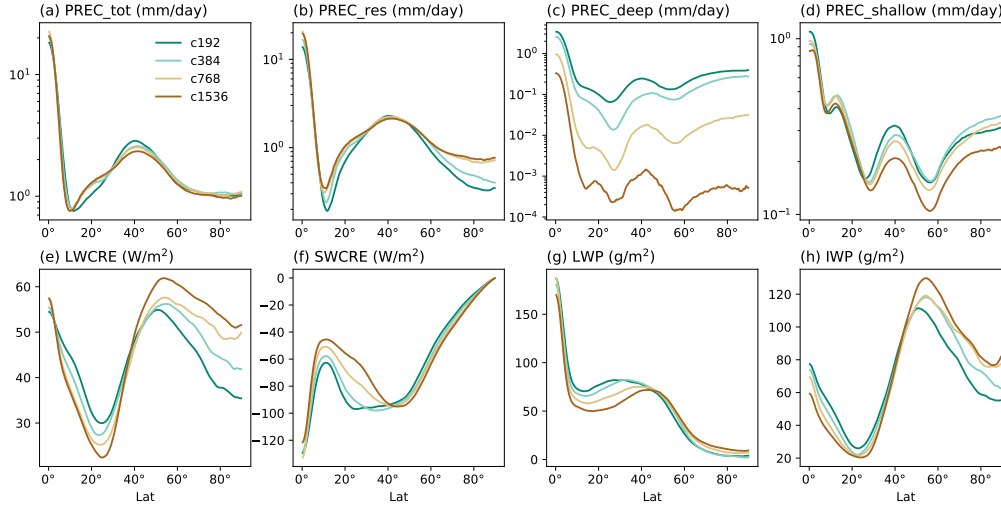


**Figure 1.** Zonal mean hemispherically-averaged climatology of (a) total precipitation, (b) precipitation at the resolved scale, (c) precipitation from the parameterized deep convection, (d) precipitation from the parameterized shallow convection, (e) longwave cloud radiative effect, (f) shortwave cloud radiative effect, (g) cloud liquid water path, and (h) cloud ice water path.

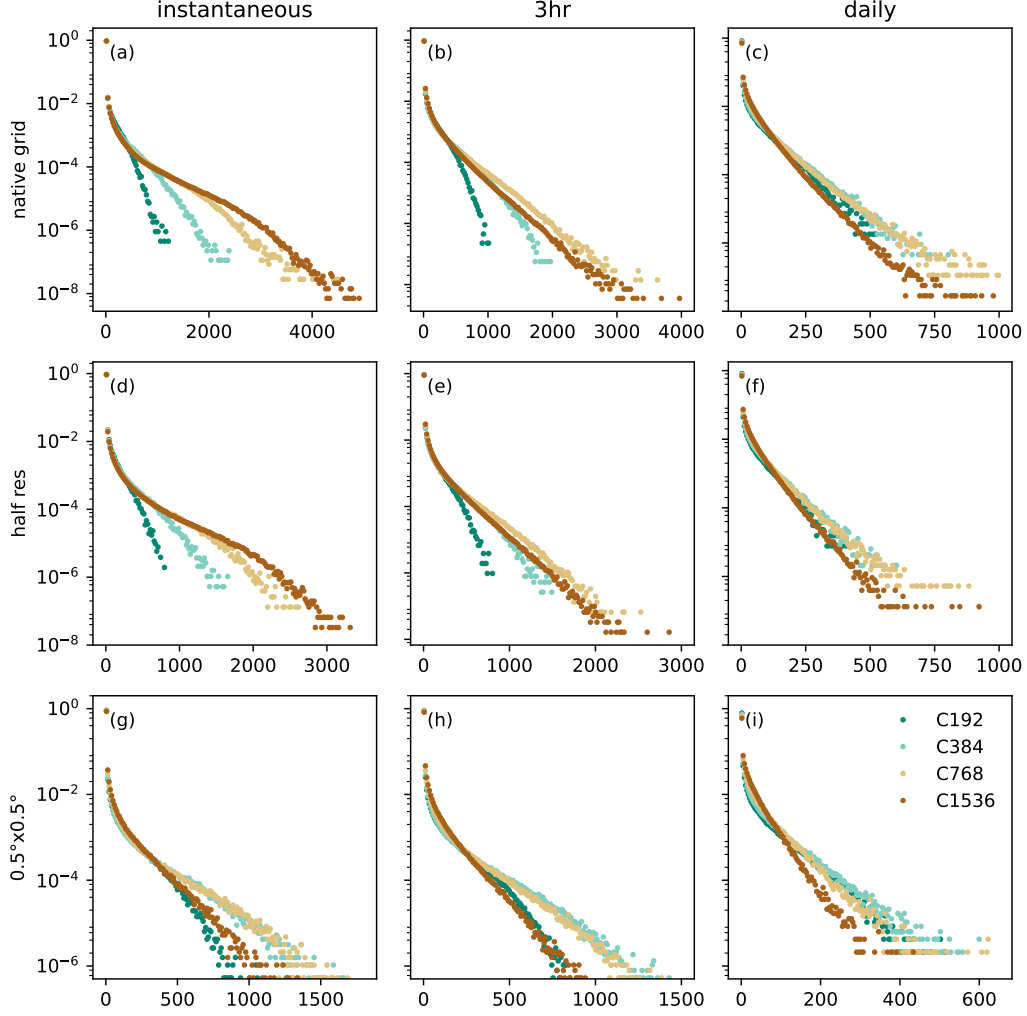


**Figure 2.** Normalized distribution of resolved precipitation intensity calculated from (a) instantaneous data at the native model grid, (b) 3 hourly averaged data at the native model grid, (c) daily averaged data at the native model grid). (d-f) As in (a-c) except that precipitation conservatively remapped to  $1^\circ \times 1^\circ$  for C192,  $0.5^\circ \times 0.5^\circ$  for C384,  $0.25^\circ \times 0.25^\circ$  for C768 and  $0.125^\circ \times 0.125^\circ$  for C1536. (g-i) As in (a-c) except that precipitation is conservatively remapped to  $0.5^\circ \times 0.5^\circ$  grid. Precipitation is in units of mm/day. All histograms are in unit of 1.

lat-lon grid varies with location, but we treat them equally when calculating distribution.

We first calculate the probability distribution of the resolved precipitation intensity and explore how it is affected by spatial and temporal sampling. We considered three temporal samplings: instantaneously every 6 hours, 3 hour mean, and daily mean; as well as three spatial samplings: at native model grid, remapped to a lat-lon grid that is roughly half of the model grid resolution, and remapped to  $0.5^\circ \times 0.5^\circ$  lat-lon grid. The time averaging is done for all time step and is equivalent to the accumulated precipitation. The spatial remapping employs a conservative algorithm (available in Open Research). As shown in Fig. 2, the intensity of the extreme precipitation is sensitive to the sampling method. We see a stronger extreme in the finer resolution simulations for instantaneously

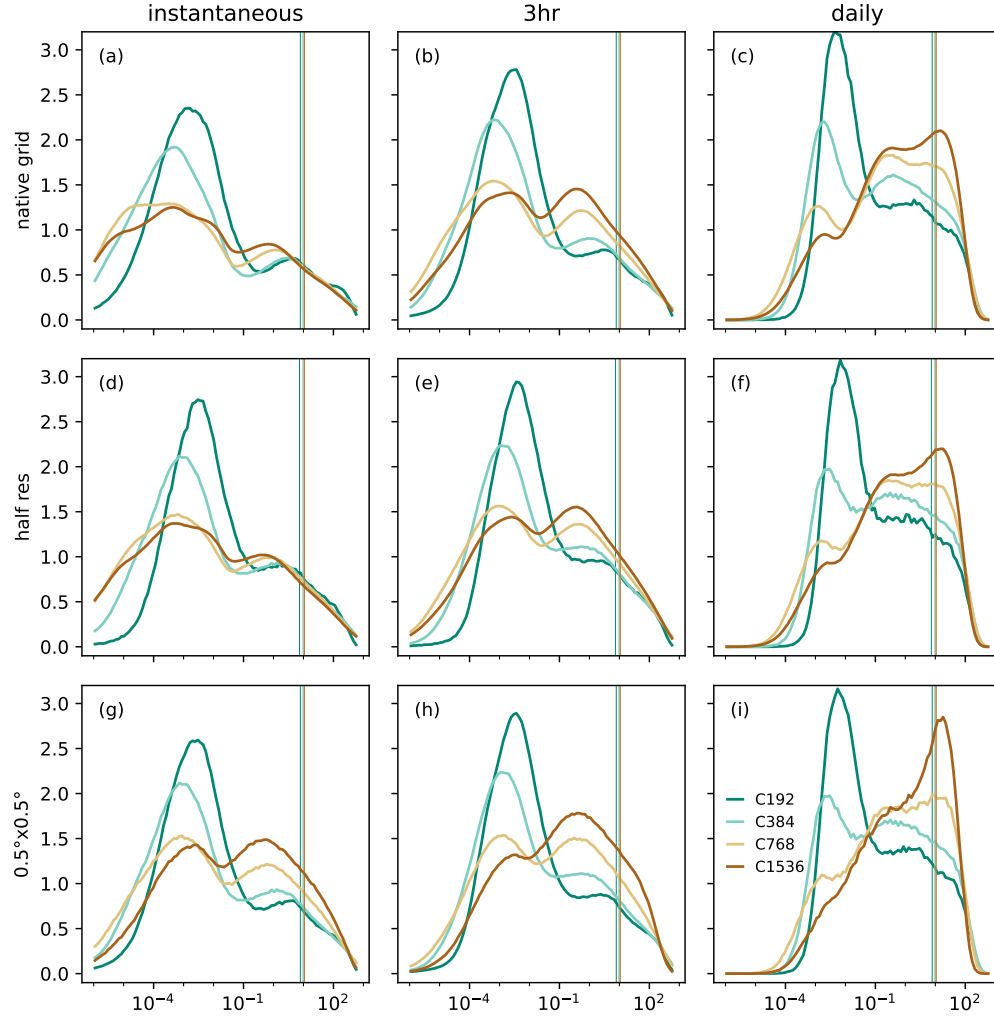


**Figure 3.** As in Fig. 2 but the histograms are calculated over 100 bins spaced evenly on log scale between  $10^{-6}$ - $10^{2.8}$  mm/day. The thin vertical lines marked the averaged values from all samples. All histograms are in units of %.

precipitation at the native model grid (Fig. 2a), which is consistent with earlier studies (Herrington & Reed, 2020). However, such resolution dependence does not hold for instantaneous precipitation remapped to the  $0.5^\circ \times 0.5^\circ$  grid (Fig. 2g). Similarly, averaging in time also distorts the resolution dependence in the extreme precipitation. For 3 hourly averaged resolved precipitation, similar distribution is found among C384, C768 and C1536 runs, whereas C192 shows a shorter tail than other (Fig. 2b). All four simulations show similar intensity for extremes in the daily averaged precipitation (Fig. 2c). When coarse-graining is done in both space and time, it is C1536, the highest resolution run, that shows the weakest extreme (Fig. 2i). Unlike earlier studies reporting that the stronger extremes in finer resolution simulation persist with coarse-graining and daily averaging (Li et al., 2011; Wehner et al., 2014; O'Brien et al., 2016; Rios-Berrios et al., 2020), we find an absence and even a reversal of the resolution dependence in the daily precipitation extremes.

To illustrate changes in the resolved precipitation at weaker intensity, we calculate the probability distribution over log-scaled bins. We find that the distributions in the high resolution runs are sensitive to the temporal and spatial averaging. For C768 and C1536 simulations, the instantaneous resolved precipitation at the native model grid shows a relatively flat distribution across all bins (Fig. 3a). Both remapping to the  $0.5^\circ \times 0.5^\circ$  grid (Fig. 3g) and daily averaging (Fig. 3c) lead to a narrower distribution and a higher mode value. Applying both spatial coarse-graining and daily averaging results in a distinct single peak located near the mean values (Fig. 3j). On the other hand, the spatial and temporal averaging has less effect on the low resolution simulations. The distribution function of C192 shows similar structure for the different sampling strategies considered here, that is a strong peak centered between  $10^{-3}$  and  $10^{-2}$  mm/day and a much muted secondary peak centered between 1 and 10 mm/day. As a result, the temporally and spatially coarse-grained resolved precipitation shows a robust resolution dependence that the finer resolution simulations produce more precipitation stronger than 0.1mm/day and less weaker precipitation.

Our simulations clearly show that the intensity distribution of the resolved precipitation depends on the sampling and the higher resolution simulations show a stronger sensitivity to the sampling method. Both the conservative spatial remapping and temporal averaging considered here effectively take an average of the samples within a subset. If the variation within each subset is comparable to the variation among all samples, then averaging of a subset yields a value similar to the all-sample mean, and the resulting distribution of the re-sampled data will be a delta function centered at the all-sample mean value. On the other hand, If the variation within the subset is small, the re-sampled data would have a similar distribution to the raw data. Here, a  $0.5^\circ \times 0.5^\circ$  grid roughly corresponds to 1 C192 model grid, but 64 C1536 model grids. Naturally, there is stronger variance within each  $0.5^\circ \times 0.5^\circ$  subset for the C1536 run than the C192 run. Correspondingly, the spatial remapping of the C1536 data leads to a large reduction of the extreme (Fig. 2 a vs g) and narrowing of the distribution (Fig. 3 a vs g), while the same remapping has little impacts on the C192 data. What is less expected is that the finer resolution runs shows a stronger sensitivity to the temporal averaging as well, which implies a resolution dependence in the temporal variance. To measure the sub-daily variance, we calculate the correlation between the daily mean precipitation and the instantaneous at the first time step of each day. The correlation is calculated over all days and all native model grid points considered here. A strong correlation of 0.71 is found for C192, indicating sampling the data instantaneously would not differ too much from the daily average. This correlation decreases monotonically with resolution, coming to 0.57 for C384, 0.44 for C768, and 0.36 for C1536, confirming that stronger sub-daily variance is simulated in models of finer resolution. While a smaller time step is used in the finer resolution runs, the physical time step in all simulations are much smaller than the time averaging length (1 day). We therefore suspect that the more time steps per day in the high resolution runs are not the main reason for the stronger sub-daily variance.



**Table 3.** Statistics of the deep tropical precipitation, gross upward mass flux ( $M_{up}$ ) and gross upward moisture flux (Q flux) evaluated using the instantaneous variables at the native model grids over the region 5.56°N-5.56°S for the 6th month. The precipitation area is defined as the fraction of grids where non-zero precipitation occurs. The ascent area is defined as the fraction of grids where the vertical velocity is larger than 0.

		C192	C384	C768	C1536
mean precip (mm/day)	total	11.25	12.11	12.06	11.60
	resolved	7.87	9.59	10.64	10.63
	deep	2.49	1.71	0.58	0.22
	shallow	0.89	0.81	0.83	0.75
precip area (%)	total	99.66	99.21	98.53	98.27
	resolved	99.53	98.83	97.87	97.72
	deep	49.51	40.39	13.36	4.25
	shallow	51.82	55.19	55.47	50.72
848.8 hPa	ascent area (%)	59.96	55.67	51.12	49.79
	$M_{up}$ ( $\times 0.01$ kg/m <sup>2</sup> /s)	1.57	1.99	2.69	3.54
	Q flux ( $\times 10^{-4}$ kg/m <sup>2</sup> /s)	2.12	2.68	3.56	4.66
532.5 hPa	ascent area (%)	45.06	45.79	46.71	47.18
	$M_{up}$ ( $\times 0.01$ kg/m <sup>2</sup> /s)	1.21	1.52	1.89	2.41
	Q flux ( $\times 10^{-4}$ kg/m <sup>2</sup> /s)	0.68	0.82	0.96	1.19

Instead, the intrinsic time scale of the precipitation variance changes with model resolution. In other words, resolving the high frequency variance is not limited by the model's time step but by the grid size since the high frequency variance are often of small spatial scales.

For completeness, we also calculate the distribution of the total precipitation and the parameterized precipitation from the deep and shallow plumes shown in Fig. 4. For simplicity, we only show the distribution using the instantaneous data at the native model grid and daily averaged coarse-grained data. At the native model grid, the deep plume precipitation intensity shows a similar mode across resolutions, but the fraction of model grids with non-zero deep plume precipitation drastically reduced (Fig. 4h). As listed in Table 3, the deep plume precipitation area decreases from 49.5% in C192 to 4.2% in C1536. The distribution of the shallow plume precipitation generally shows little sensitivity to varying resolution, except that C192 shows a slightly wider range than others. The extremes of the combined precipitation from both resolved and parameterized processes largely come from the resolved precipitation and thus show a similar sensitivity to resolution (Figs. 4a vs 2a, 4d vs 2i).

### 3.3 Relationship between the resolved precipitation and vertical velocity

Previous studies have attributed the resolution dependence in the resolved precipitation to changes in the vertical velocity amplitude (Rauscher et al., 2016; Herrington & Reed, 2017, 2020). The strongest vertical velocity intensifies at finer resolutions, which produces a stronger gross upward moisture flux at the cloud base. The resolved precipitation is found to be proportional to the gross upward moisture flux (Rauscher et al., 2016; O'Brien et al., 2016; Herrington & Reed, 2020). Therefore, an intensification of the strongest precipitation is expected following the intensification of the strongest ascent. Herrington and Reed (2020) further showed that the enhancement of the mean resolved precipitation in simulations of higher resolution mainly comes from precipitation of the strongest intensity that is co-located with the strongest upward motion.

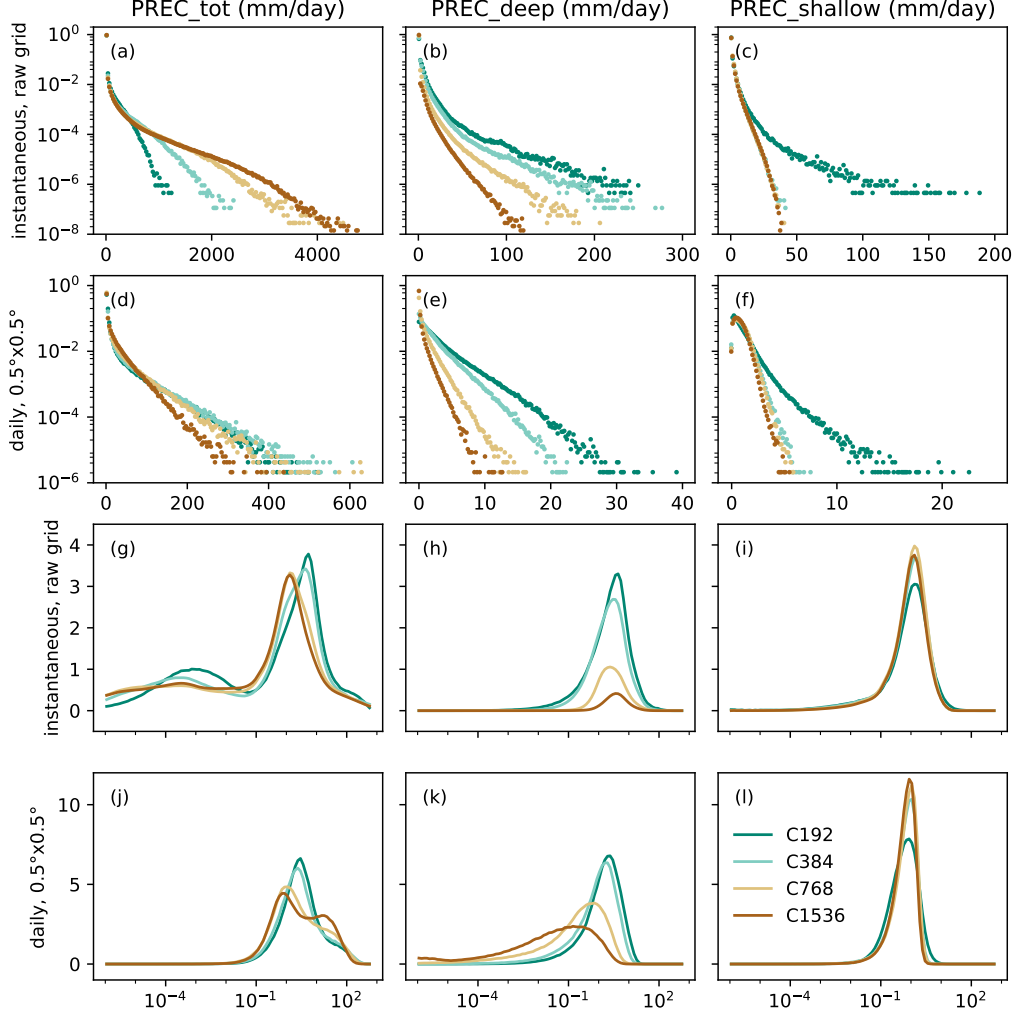


**Figure 4.** Normalized distribution of (a, d, g, j) total precipitation intensity, (b, e, h, k) parameterized precipitation from the deep plume, and (c, f, i, l) parameterized precipitation from the shallow plume. (a-c) Distribution is calculated using instantaneous data at the native model grid over 200 bins spaced evenly on linear scale. (d-f) As in (a-c) but using daily averaged data conservatively remapped to  $0.5^\circ \times 0.5^\circ$  grid. (g-i) Distribution is calculated using instantaneous data at the native model grid over 100 bins spaced evenly on log scale. (j-l) As in (g-i) but using daily averaged data conservatively remapped to  $0.5^\circ \times 0.5^\circ$  grid.

We verify this argument in our simulations over the deep tropics. Table 3 lists the gross upward mass flux, the gross upward moisture flux along with the areal averaged precipitation. These quantities are calculated from the instantaneous fields sampled at the native model grid. Consistent with earlier studies (Herrington & Reed, 2017, 2020), stronger gross upward mass flux and stronger gross upward moisture flux are found at the cloud base level as well as at mid-troposphere in simulations of finer resolution. Each resolution doubling leads to roughly 30% increase in the upward mass flux at 848.8 hPa, and roughly 25 % increases at 532.5 hPa. This stronger upward mass flux does not come from changes in the ascent area but is driven by the stronger intensity of the vertical velocity. The gross upward moisture flux generally scales with the mass flux, confirming that changes in the moist flux is driven by the vertical velocity. The resolved precipitation, on the other hand, does not scale with the upward mass flux or the moisture flux. It increases by 22% when the resolution doubles from C192, but only 11% for the second resolution doubling, and decreases slightly for the third resolution doubling. Such disproportion between resolved precipitation and vertical velocity is also seen in the extreme and mode values as evident in Fig. 5a vs Fig. 2a and Fig. 5b vs Fig. 3a.

To probe into the relationship between the vertical velocity and the resolved precipitation, we sort the data points according to the vertical velocity and calculate the fraction of data points and the mean resolved precipitation in each bin, denoted as  $f_i$  and  $P_i$ , respectively. The temporal and areal averaged precipitation over the deep tropics can be written as the sum over bins:  $P = \sum_i f_i P_i$ . We further calculate  $f_i \langle P_i \rangle$  and  $\langle f_i \rangle P_i$ , where  $\langle \rangle$  indicates the average among the 4 experiments. Comparing  $f_i \langle P_i \rangle$  and  $\langle f_i \rangle P_i$  answers the question whether changes in the precipitation are driven by changes in the vertical velocity intensity. Similar decomposition is carried out by Terai et al. (2018) and Herrington and Reed (2020). As shown in Fig. 6a, the resolution dependence of precipitation is contributed by both strong and weak ascent bins. Changes in the strong ascent bins mainly comes from a larger fraction of grid points in those bins with strong ascent, but the mean precipitation in those bins changes little with resolution. This is consistent with the aforementioned mechanism and the results shown by Herrington and Reed (2020). Change in the weak ascent bins, on the other hand, mainly comes from a weaker mean precipitation intensity in those bins rather than changes in  $f_i$ . Changes in  $f_i$  alone lead to a  $\sim 30\%$  increase of the deep tropical mean precipitation from each resolution doubling (Fig. 6c), which is consistent with changes in the gross upward mass flux and the gross upward moisture flux listed in Table 3. This is compensated by changes in  $P_i$  over weak ascent bins, and the actual resolved precipitation response to resolution is much more muted, especially for simulations at finer resolutions.

Similar calculations are done for the daily averaged coarse-grained data. Note that the daily averaged coarse-grained vertical velocity is different from the averaged upward motion. The discrepancy between the two is small for the extreme strong ascent but large for mean weak ascent. As shown in Fig. 6d, varying resolution mainly affects precipitation in bins with weak vertical velocity but not in bins with strong ascent. The larger contribution to precipitation under the weak vertical velocity condition in higher resolution simulations is brought by the stronger precipitation intensity sampled at the same vertical velocity. On the other hand, the fraction of data points in each vertical velocity bin is similar among simulations except for C1536, which shows larger fraction in weak velocity bins and smaller fraction in strong velocity bins (Fig. 6f). This precipitation decomposition using the coarse-grained data is consistent with results by Terai et al. (2018), who reported that the resolution dependence in the resolved precipitation mainly comes from changes in the precipitation irrespective to vertical velocity. This breakdown based on the daily averaged coarse-grained data highlights the precipitation changes over weak ascent regions, which cannot be explained by the resolution dependence in the vertical velocity amplitude.

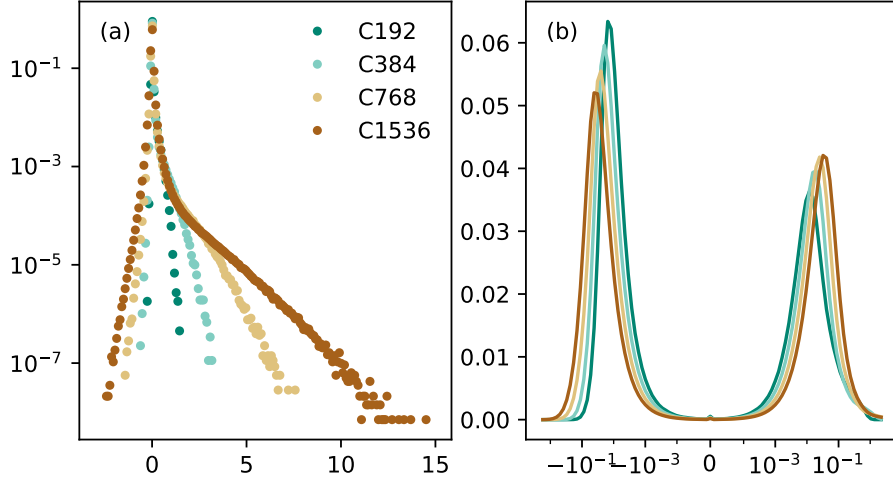


**Figure 5.** Normalized distribution of vertical velocity at 532 hPa sampled instantaneously every 6 hours at the native model grid (a) over 200 bins spaced evenly on linear scale between -3 and 15 m/s in units of 1, (b) over 50 bins spaced evenly on log scale between  $-10^{0.4}$  and  $-10^{-4}$  m/s and 50 bins between  $10^{-4}$  and  $10^{0.4}$  m/s in units of %.

### 3.4 Precipitation organization in the deep tropics

We examine the organization of precipitation and its associated circulation in the deep tropics. We use daily averaged data coarse-grained to the  $0.5^\circ \times 0.5^\circ$  grid over the entire 9 months after spin-up. The precipitation is further averaged over  $5^\circ\text{N}$  and  $5^\circ\text{S}$ . As will be shown below, the dominant variance after these temporal and spatial averaging is mostly Kelvin wave.

Figure 7 shows the Hovmöller plot for precipitation averaged over  $5^\circ\text{N}$ - $5^\circ\text{S}$ . In all experiments, the eastward propagating Kelvin waves is manifested in the parallel stripes of strong precipitation in the Hovmöller plots. The dominance of the Kelvin waves is confirmed in the space-time spectra of precipitation and OLR shown in Fig. 8. The eastward propagating Kelvin waves are readily seen in both resolved and parameterized precipitation. The phase speed of the Kelvin wave indicated by the slope of the precipitation stripes are similar among different experiments and precipitation components. In the C192 experiment, the resolved precipitation shows localized extreme intensity, and the precipitation stripe is frequently interrupted. These popcorn-like pockets are greatly suppressed as the resolution increases, and the precipitation stripes become smoother and more continuous (Fig. 7e-h). The smoother precipitation stripes at the finer resolution are also seen in the precipitation from the parameterized deep plume (Figs. 7i-l) and shallow plume (Figs. 7m-p). The suppression of the popcorn pockets and the more continuous precipitation indicate a stronger role of the large-scale circulation.

This transition from the localized popcorn convection to the more organized convection is evident in the one-point correlation maps against the equatorial precipitation. The correlation is calculated as:

$$r(\theta, \Delta\phi) = \frac{[(x(t, \theta, \phi + \Delta\phi) - [x])(y(t, \phi) - [y])]}{\sqrt{[(x - [x])^2]} \sqrt{[(y - [y])^2]}}$$

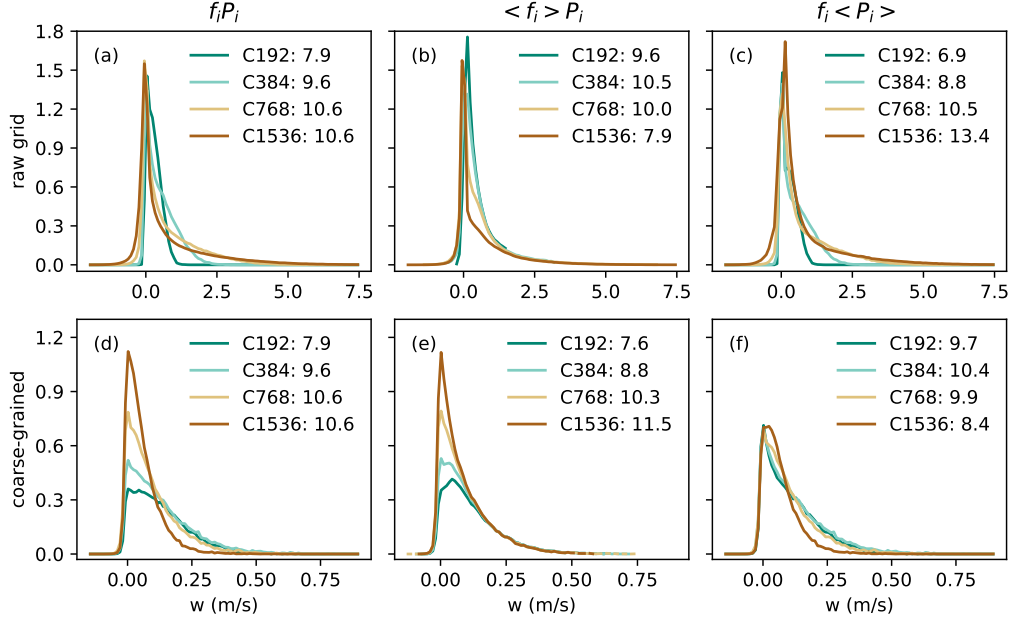


**Figure 6.** (a) Resolved precipitation amount binned with respect to the vertical velocity at 532 hPa evaluated using the instantaneous data at the raw model grid. It is calculated as the product of the mean precipitation intensity in each bin  $P_i$  and the fraction of data points in each bin  $f_i$ . The sum of  $f_i P_i$  from each experiment is listed in the legend, corresponding to the monthly mean areal mean resolved precipitation intensity in units of mm/day. The vertical velocity is divided into 100 bins linearly ranging from -2 m/s to 7.5 m/s. (b) As (a), but assuming a common fractional distribution among vertical velocity bins  $\langle f_i \rangle$  for all experiments. (c) As (a), but assuming a common mean precipitation intensity in each vertical velocity bin  $\langle P_i \rangle$  for all experiments. (d)-(f) As (a)-(c) except for using the daily mean coarse-grained data and the vertical velocity is divided into 100 bins linearly ranging from -0.15 m/s to 0.9 m/s.

where  $x$  is the variable,  $y$  is the equatorial precipitation averaged over  $5^{\circ}\text{N}$ - $5^{\circ}\text{S}$ ,  $t$  is time,  $\theta$  is latitude,  $\phi$  is the reference longitude,  $\Delta\phi$  is the longitudinal distance from the reference, and  $[\ ]$  indicates a zonal mean over all longitudes and time mean over the entire 9 months after spin-up.

Since the variance of this precipitation index is dominated by strong intensities, the one-point correlation maps show how precipitation is organized around a local precipitation maximum, which often results from a deep convection core. Note that the relative distance in longitude is equivalent to the relative sequence in time here given that the eastward moving Kelvin wave is the dominant variance. Features found to the east of the deep convection core (relative longitude  $> 0$ ) occur prior the deep convection, and vice versa.

In the C192 experiment, high correlation is found at the same location where the precipitation index is defined, but near-zero correlation is found anywhere else. This is consistent with the localized popcorn convection seen in Figs. 7a, 7e, 7i, 7m. As the resolution increases, correlations start to emerge outside the location where the precipitation index is defined. The longitudinal scale of the correlation patterns becomes wider and the non-local correlations becomes stronger. These non-local correlations indicate modulations from the large-scale circulation associated with the deep convection. At the resolution of C1536, the correlation maps of the total (Fig. 9d) and the resolved precipitation (Fig. 9h) show a Gill-type response to the deep convection (Gill, 1980): positive correlation is found over a tongue extending to the east of the deep convection core and a pair of patches centered off-equator to the west. Negative correlations are found along the equator, corresponding to the descending branch of the Gill-type circulation anomaly. The precipitation from the parameterized deep and shallow plumes both show a pattern of zonal wave number 1. For the deep plume (Fig. 9l), stronger parameterized precipitation is found to the west or after the deep convection core. Contrarily, the shallow plume produces stronger precipitation to the east or prior of the deep convection core (Fig. 9p).

To examine the organization in the circulation associated with the precipitation, we calculate similar one-point correlation maps between the precipitation index and various variables. As shown in Figs. 11 and 10, all these one-point correlation maps show stronger non-local correlations as the model resolution increases. A longitudinal expansion is evident as resolution increase from C192 to C384, though further expansions are more subtle for higher resolutions. These common features among all variables indicate a robust sensitivity in the organization state of the equatorial convection to the model resolution. In particular, we see a closer relationship between the large-scale circulation and the deep convection core at finer resolution, which provides more favorable conditions for convection organization.

A common structure seen in all convective coupled equatorial waves is the shallow convection occurring prior the deep convection and the stratiform clouds and precipitation trailing the deep convection, which distinguish them from the isolated unorganized convection (Kiladis et al., 2009, and references therein). This shallow-to-deep-to-stratiform transition is associated with a slantwise circulation as well as vertical displacement of convective and radiative heating, which all contribute to the maintenance and propagation of convective waves. Similar shallow-to-deep-to-stratiform transition is also important for the mesoscale convective systems (MCSs) (e.g., Houze, 2004; Moncrieff, 2010). Properly simulating this shallow-to-deep-to-stratiform transition is therefore crucial for simulating these equatorial waves and the organized convective system in general (e.g., Frierson et al., 2011; Seo et al., 2012). Such transition is clearly manifested in vertical velocity (Figs. 10a-b), cloud fraction (Figs. 10e-h), relative humidity (Figs. 10i-l) and moist static energy (MSE; Figs. 10m-p). We see that on the east side of the deep convection core, the lower troposphere is moist and of high MSE, upward motion is largely confined within the lower troposphere and clouds are forming below  $\sim 750$  hPa, all of which indicate shallow convection. On the west side of the deep convection core, MSE and hu-



midity are higher over the upper troposphere than the lower troposphere, and upward motion and clouds are found over the upper troposphere, signaling the stratiform phase. The parameterized convection also contribute to the shallow-to-deep-to-stratiform transition as indicated by the convective mass flux from the deep plume (Figs. 10q-t) and the shallow plume (Figs. 10u-x). The parameterized shallow plume varies inversely with the convective inhibition (CIN) in our model, which is tightly linked to the low level humidity. Thus, the high low-level relative humidity prior the deep convection indicates a low CIN and a stronger shallow plume from the parameterization. In the deep plume parameterization, the fractional lateral mixing rate decreases with the free troposphere column relative humidity. Higher free troposphere relative humidity is found at the deep convection core and over the stratiform region, which reduces lateral mixing there and promotes a stronger deep plume.

We further show the one-point correlation on the latitude-longitude plane in Fig. 11. The low surface pressure anomalies to the east of precipitation and high anomalies to the west (Figs. 11e-h) are consistent with the theoretical prediction for the equatorial Kelvin waves (Matsuno, 1966). OLR anomalies (Figs. 11a-d) largely reflect the clouds anomalies associated with convective system: low OLR anomalies come from the stratiform anvil clouds and high OLR anomalies are found over the region where there is little high clouds. The column-integrated MSE anomalies (Figs. 11i-l) are dominated by moisture anomalies over the lower troposphere, showing high MSE anomalies prior precipitation at the equator. Similar to the one-point correlations shown above, all three variables show a clear longitudinal expansion with resolution. On the other hand, the latitudinal scales of these precipitation-associated anomalies do not vary much with resolution.

All the variables shown in Figs. 9, 10 and 11 manifest a robust resolution dependence in the convective organization. The shallow-to-deep-to-stratiform transition is barely discernible in the C192 run but expands to a much wider system in longitudes at the finer resolutions, and the non-local effects of the convection becomes stronger as the resolution increases. Whether the convection is dominated by the organized system or the unorganized popcorn would lead to different relationship between precipitation and the local vertical velocity. For a localized convection, strong ascent is always co-located with strong precipitation. For a convective system, strong precipitation and strong ascent are found at the deep convection core, but precipitation also forms over the shallow convection and stratiform region, which is less controlled by the local vertical velocity. As the model resolution increases, the convective system becomes stronger, and more moderate precipitation forms over the shallow and stratiform region, which might explain the precipitation changes irrespective of vertical velocity seen in Fig. 6e.

Note that the zonal wavenumber-1 structures apparent in these one-point correlation maps are not contradictory to spectra analysis showing power over a range of zonal wavenumbers (Fig. 8). This is because precipitation does not vary along longitude as a sinusoidal wave but more as individual solitons. Fourier transform of a single soliton project powers on a range of zonal wavenumbers. It is also worth noting that the stronger organization at finer resolution is not only contributed by the resolved processes but by the parameterized ones as well, despite the fact that the cumulus parameterization here is not directly “scale-aware”. These resolution dependence in the parameterized convection reflects the modulation of the large-scale circulation to the parameterized convection via the mean states, mostly the relative humidity.

## 4 Summary and discussion

We performed a series of aquaplanet simulations using the GFDL AM4-MG2 model with horizontal resolution ranging from 50km to 6km. As the resolution increases, the globally averaged precipitation at the resolved scale intensifies while the precipitation

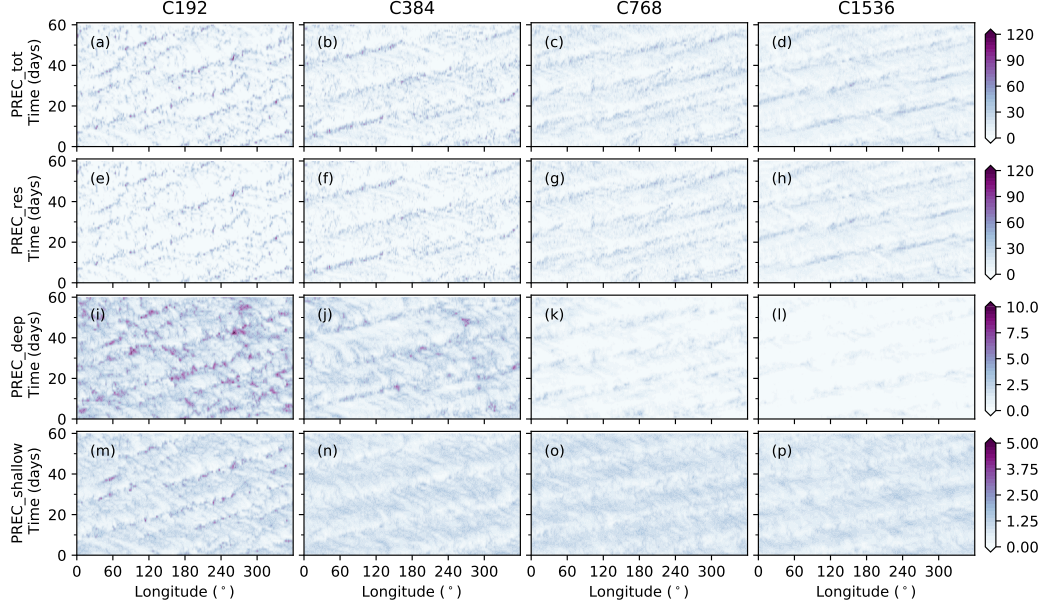


**Figure 7.** Hovmöller plot of daily mean precipitation averaged over  $5^{\circ}\text{N}$ - $5^{\circ}\text{S}$  over the 6th and 7th months for (a-d) total precipitation, (e-h) resolved precipitation, (i-l) parameterized deep plume precipitation, and (m-p) parameterized shallow plume precipitation. (a, e, i, m) show results for C192, (b, f, j, n) for C384, (c, g, k, o) for C768, and (d, h, l, p) for C1536. Precipitation is in units of mm/day.

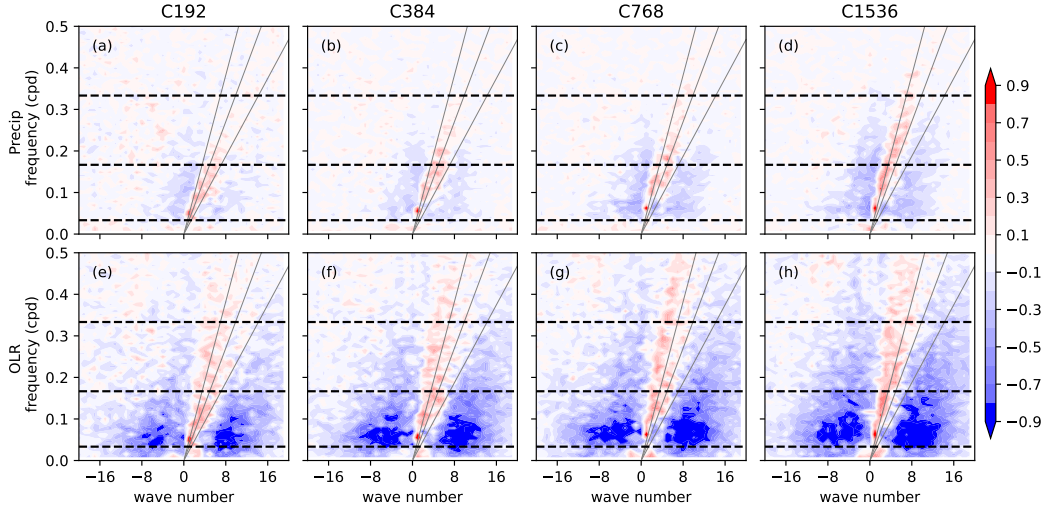


**Figure 8.** The 10 base logarithm of the ratio between the symmetric component and the background spectra in (a-d) total precipitation, and (e-h) OLR following Wheeler and Kiladis (1999). The spectra is calculated using the daily mean coarse-grained data over  $15^{\circ}\text{N}$ - $15^{\circ}\text{S}$  over the entire 9 months. The gray lines indicate the theoretical dispersion relationship for Kelvin waves corresponding to equivalent depths of 12, 25, and 50 m. The black dashed lines mark the period of 3, 6 and 30 days. (a, e) show results for C192, (b, f) for C384, (c, g) for C768 and (d, h) for C1536.

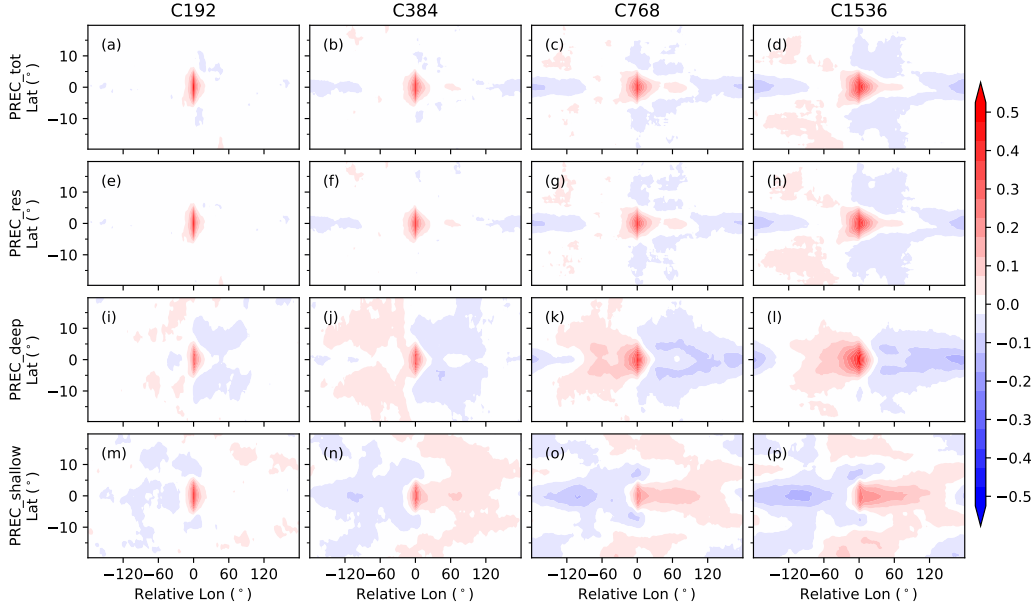


**Figure 9.** Correlation against the total precipitation averaged over  $5^{\circ}\text{N}$ - $5^{\circ}\text{S}$  at a reference longitude for (a-d) total precipitation, (e-h) precipitation at the resolved scale, (i-l) precipitation from the parameterized deep plume, and (m-p) precipitation from the parameterized shallow plume. (a, e, i, m) show results for C192, (b, f, j, n) for C384, (c, g, k, o) for C768, and (d, h, l, p) for C1536.

produced by the cumulus parameterization weakens. This is consistent with earlier studies using models of resolutions coarser than 25km (e.g., Wehner et al., 2014; Herrington & Reed, 2017; Terai et al., 2018; Herrington & Reed, 2020). The resolved precipitation seems to approach convergence for resolutions finer than 13km in our simulations, especially over the deep tropics. The precipitation from the parameterized deep plume decreases by an order as the resolution increases from 50km to 6km, while variations in the shallow plume across resolution are generally weak. More and/or thicker clouds are simulated at the finer resolution over high latitudes, and less and/or thinner clouds are found over low latitudes.

Studies have attributed the enhancement of the mean resolved precipitation with resolution to the intensification of the extreme precipitation, which is linked to the intensification of the strongest ascent (Rauscher et al., 2016; O’Brien et al., 2016; Herrington & Reed, 2017, 2020). Our simulations at higher resolution suggest that the resolution dependence in the resolved precipitation cannot be fully explained by the intensification of the strongest ascent. Changes in the precipitation with resolution occurs not only over the extreme intensity range but also over weak and moderate intensity range and outside of the strongest ascent region. Intensification of the extreme precipitation with resolution is only seen in instantaneous samples but not in the daily averaged one. We report a robust resolution sensitivity in the convective organization state in our model, which has not been reported in previous GCM studies. A stronger correlation is found between the local precipitation event and the large-scale circulation in simulations at finer resolution. As the large-scale convective system takes over, the localized popcorn convection is suppressed, moderate precipitation is enhanced, but the extreme precipitation is less affected.

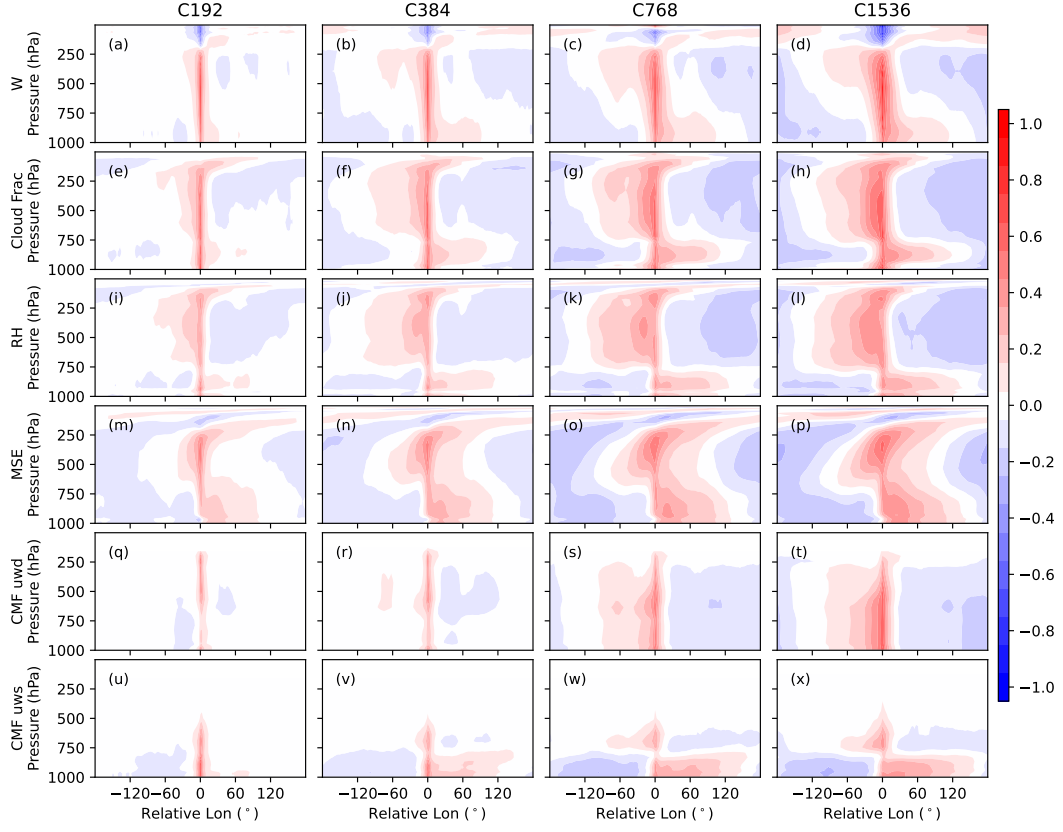


**Figure 10.** As Fig. 9, except for (a-d) vertical velocity, (e-h) cloud fraction, (i-l) relative humidity, (m-p) moist static energy, (q-t) convective mass flux from the parameterized deep plume, and (u-x) convective mass flux from the parameterized shallow plume. All variables are averaged over 5°N-5°S.

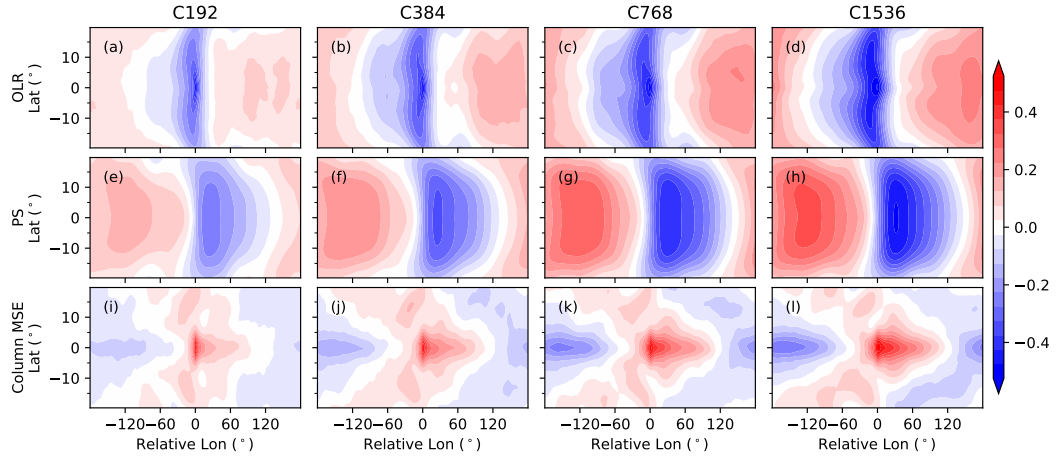


**Figure 11.** As Fig. 9, except for (a-d) OLR, (e-h) surface pressure, (i-l) column integrated moist static energy.

We show that the precipitation extremes and intensity distribution simulated in the higher resolution model is strongly affected by whether precipitation has been spatially coarse-grained and/or averaged over time, whereas the lower resolution models show less sensitivity to the re-sampling. This explains why earlier GCM studies at the resolution lower than 25km reported similar resolution dependence in extreme precipitation regardless of whether data is sampled at native model grid or coarse-grained, instantaneously or daily averaged (e.g., Li et al., 2011; Wehner et al., 2014; O’Brien et al., 2016; Rios-Berrios et al., 2020; Herrington & Reed, 2020). On the other hand, recent model studies at higher resolutions reported distinction between extremes in instantaneous and daily precipitation (Bao & Sherwood, 2018; Bao & Windmiller, 2021; O’Gorman et al., 2021).

Besides model resolution, the precipitation extremes and convective organization are also sensitive to the diffusive damping setting in the dynamical core. Anber et al. (2018) evaluated the sensitivity in convection organization and precipitation extremes to the damping settings in a radiative-convective equilibrium (RCE) configuration based on the same FV3 dynamical core used here. They found a weaker damping setting (either by using a higher order damping or a weaker damping coefficient) leads to weaker extremes in the 6-hourly averaged precipitation. As discussed in the appendix, the dynamical core setting in our simulations may be too diffusive for the finer resolution runs. If higher order damping and/or weaker damping coefficients to be used in the finer resolution runs, we expect the daily precipitation extremes to reduce even more in the finer resolution runs, leading to a further departure from the estimation based on vertical velocity. On the other hand, the simulations by Anber et al. (2018) are limited to a small domain of 32km x 32km so that convective organization on the larger scales are ignored. The sensitivity to diffusion settings found in their model may not hold in a global simulation. Given the complex coupling across different scales, how artificial diffusion affects convection in a global model may be counter-intuitive as discussed by Zhao et al. (2012).

This work highlights the complexity to understand the global simulations at the convective gray zone resolution, where the underlying physics may be different from the conventional GCMs or the cloud-resolving models and the Large Eddy Simulations (LES) of limited domain. Since it remains challenging to run the global simulation at a resolution fully resolving convection and clouds in the foreseeable future, more investigations are called for to understand the resolution dependence and the interaction between the parameterized and resolved convection at the convective gray zone resolution.

## Appendix A Diffusion Settings

Numerical diffusion is an indispensable component of the dynamical core, representing the viscous dissipation of kinetic energy cascading towards molecular scales by the unresolved turbulent eddies. This is achieved implicitly from the advection operator as well as explicitly by adding artificial damping. Choices of these diffusion settings would certainly affect the characteristics of the simulated circulation. A detailed documentation of the numerical diffusion settings in the FV3 dynamical core as well as guidelines for choosing these diffusion settings can be found in Harris et al. (2021, Chapter 8). Here, we provide a short summary of the diffusion settings used in our simulations.

We use a monotonic operator for advection in our simulations, which is more diffusive than the unlimited or positive-definite operators. More specifically, we use the third-order piecewise-parabolic method with the “fast monotonicity constraint” of S.-J. Lin (2004) for tracers. Horizontal advection of momentum, vorticity, potential temperature and mass uses the quasi-monotone constraint proposed by Huynh (1997), which is significantly less diffusive than the one used for tracers. For the explicit damping, we use separate damping on the divergent and rotational components of the flow. The diver-



gence damping is applied to horizontal winds as following:

$$\mathbf{v}^{n+1} = \mathbf{v}^n + \dots + (-1)^N \nu_D \frac{\delta_x(\nabla^{2N} D)}{\Delta \mathbf{x}}$$

where  $\mathbf{v}$  is the vector of horizontal wind,  $n$  is the time index,  $\delta_x$  is a centered-difference operator,  $D$  is the divergence of horizontal winds,  $\Delta \mathbf{x}$  is the horizontal grid length, and  $\nu_D$  is the damping coefficient.  $\nu_D$  is calculated in the model as  $(d_{2N} \Delta A_{min})^{N+1}$ , in which  $\Delta A_{min}$  is the global minimum grid-cell area and  $d_{2N}$  is a specified non-dimensional constant. Such formulation is equivalent to a  $\nabla^{2N+2}$  form of hyper diffusion for the divergence field (i.e.,  $(2N+2)$ -th order damping), and  $\nu_D/\Delta t$  is equivalent to the dimensional hyperviscosity coefficient ( $\Delta t$  is the dynamical time step). We use  $N = 1$  and  $d_{2N} = 0.15$  for all our simulations, that is a 4th order damping with hyperviscosity coefficient of  $6.32 \times 10^{14} m^4 s^{-1}$  for C192,  $1.03 \times 10^{14} m^4 s^{-1}$  for C384,  $1.10 \times 10^{13} m^4 s^{-1}$  for C768 and  $1.38 \times 10^{12} m^4 s^{-1}$  for C1536. Vorticity damping is of the same order as the divergence damping, and the vorticity damping coefficient  $\nu_v$  is calculated in a similar fashion to  $\nu_D$ , that is  $\nu_v = (d_v \Delta A_{min})^{N+1}$ . We use  $d_v = 0.02$  for all our simulations, which corresponds to a dimensional damping coefficient of  $1.12 \times 10^{13} m^4 s^{-1}$  for C192,  $1.84 \times 10^{12} m^4 s^{-1}$  for C384,  $1.96 \times 10^{11} m^4 s^{-1}$  for C768 and  $2.45 \times 10^{10} m^4 s^{-1}$  for C1536.

As discussed in Harris et al. (2021, Chapter 8), the choices of the diffusion settings should be chosen for desirable simulation features rather than objectively determined. A model with high resolution typically employs a less diffusive advection operator and a higher-order artificial damping scheme that is more scale selective, whereas a conventional climate model often employs a more diffusive advection operator and a lower-order damping scheme to improve the large-scale circulation features. But this is not always the case. The diffusion setting used in this study follows the setting used in the C192 AM4 climate simulations runs (Zhao, 2020), which choose a lower order divergence damping than in the lower resolution ones (4th order in C192 vs 6th order in C96) to improve simulations of tropical cyclones. We note that the diffusion settings here may not be the optimal choice for high resolution runs. As shown in Fig. A1, the  $k^{-5/3}$  slope in the horizontal kinetic energy spectra is barely resolved even in our high resolution simulations, suggesting that our model setting is too diffusive to fully resolve the mesoscale energy cascade. Takahashi et al. (2016) argue that the dimensional damping coefficients of a 4th order damping should scale with  $\Delta x^{3.22}$  to properly resolve the mesoscale kinetic energy, which leads to a decrease by an order of magnitude in the damping coefficient for each resolution doubling. Our explicit dimensional divergence and vorticity damping coefficients do decrease as resolution increases but not as much as the scaling proposed by Takahashi et al. (2016), which may partly explain the early departure from the  $k^{-5/3}$  slope in our simulations. However, one should note that the strength of the diffusion is not solely determined by the damping coefficients. Choices of the advection operator and the order of the damping also affect how diffusive the model is, and their effects are usually implicit, nonlinear and not straightforward to quantify. For example, a much better resolved  $k^{-5/3}$  slope is seen in simulations by the FV3 dynamical core with a less diffusive advection operator (“virtually-inviscid” scheme vs monotonic scheme), a higher order divergence damping (8th vs 4th) and a similar non-dimensional damping coefficient (e.g., S.-J. Lin et al., 2018).

## Open Research

The source code of the AM4-MG2 nonhydrostatic aquaplanet model and configurations of the simulations presented in this manuscript is available at: [doi.org/10.5281/zenodo.7476908](https://doi.org/10.5281/zenodo.7476908) (Robinson et al., 2022). The specification of the model’s vertical coordinate, analysis scripts and model outputs used in the manuscript are available at: [doi.org/10.5281/zenodo.7537434](https://doi.org/10.5281/zenodo.7537434) (P. Lin et al., 2023). The spatial remapping is done using fregrid, which is part of the FRE-NCtools, available at: <https://github.com/NOAA-GFDL/FRE-NCtools> (GFDL modeling systems group, 2022).



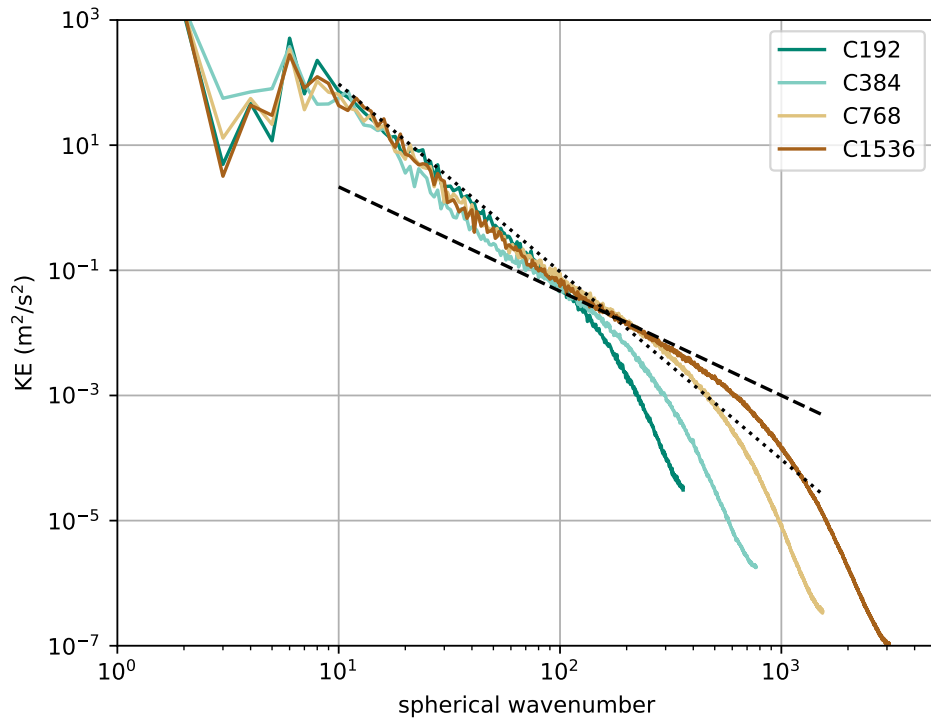


**Figure A1.** Kinetic energy spectra at 221 hPa. The dotted line indicates the  $k^{-3}$  slope and the dashed line indicates the  $k^{-5/3}$  slope.

## Acknowledgments

We thank Drs. Isaac Held, Nadir Jeevanjee, Zhihong Tan, Linjiong Zhou and Lucas Harris for their comments on an earlier version of the manuscript. We thank Rusty Benson, Linjiong Zhou, Huan Guo and Levi Silvers for their help on constructing the simulations, and Wenhao Dong for analyzing the model outputs. We thank the anonymous reviewers for their constructive comments. This report was prepared by Pu Lin under award NA18OAR4320123 from the National Oceanic and Atmospheric Administration, U.S. Department of Commerce. The statements, findings, conclusions, and recommendations are those of the author(s) and do not necessarily reflect the views of the National Oceanic and Atmospheric Administration, or the U.S. Department of Commerce. We acknowledge GFDL resources made available for this research.

## References

- Ahmed, F., & Schumacher, C. (2015). Convective and stratiform components of the precipitation-moisture relationship. *Geophys. Res. Lett.*, *42*, 10453-10462. doi: 10.1002/2015GL066957
- Anber, U. M., Jeevanjee, N., Harris, L. M., & Held, I. M. (2018). Sensitivity of radiative-convective equilibrium to divergence damping in GFDL-FV3-based cloud-resolving model simulations. *J. Adv. Model. Earth Sy.*, *10*, 1528-1536. doi: 10.1029/2017MS001225
- Arnold, N. P., Putman, W. M., & Freitas, S. R. (2020). Impact of resolution and parameterized convection on the diurnal cycle of precipitation in a global nonhydrostatic model. *J. Meteorol. Soc. Jpn.*, *98*, 1279-1304. doi: 10.2151/jmsj.2020-066
- Bao, J., & Sherwood, S. C. (2018). The role of convective self-aggregation in extreme instantaneous versus daily precipitation. *J. Adv. Model. Earth Sy.*, *11*, 19-33. doi: 10.1002/2018MS001503
- Bao, J., Sherwood, S. C., Colin, M., & Dixit, V. (2017). The robust relationship between extreme precipitation and convective organization in idealized numerical modeling simulations. *J. Adv. Model. Earth Sy.*, *9*, 2291-2303. doi: 10.1002/2017MS001125
- Bao, J., & Windmiller, J. M. (2021). Impact of microphysics on tropical precipitation extremes in a global storm-resolving model. *Geophys. Res. Lett.*, *48*. doi: 10.1029/2021GL094206
- Benedict, J. J., Medeiros, B., Clement, A. C., & Pendegrass, A. G. (2017). Sensitivities of the hydrological cycle to model physics, grid resolution and ocean type in the aquaplanet Community Atmosphere Model. *J. Adv. Model. Earth Sy.*, *9*, 1307-1324. doi: 10.1002/2016MS000891
- Blackburn, M., Williamson, D. L., Nakajima, K., Ohfuchi, W., Takahashi, Y. O., Hayashi, Y.-Y., ... Stratton, R. (2013). The aqua-planet experiment (APE): control SST simulations. *J. Meteorol. Soc. Jpn.*, *91A*, 17-56. doi: 10.2151/jmsj.2013-A02
- Bretherton, C. S., Peters, M. E., & Back, L. E. (2004). Relationships between water vapor path and precipitation over the tropical oceans. *J. Clim.*, *17*, 1517-1528. doi: 10.1175/1520-0442(2004)017<1517:RBWVPA>2.0.CO;2
- Caldwell, P. M., Terai, C. R., Hillman, B., Keen, N. D., Bogenschutz, P., Lin, W., ... Zender, C. S. (2021). Convection-permitting simulations with the E3SM global atmosphere model. *J. Adv. Model. Earth Sy.*, *13*. doi: 10.1029/2021MS002544
- Donner, L. J., Wyman, B., Hemler, R. S., Horowitz, L. W., Ming, Y., Zhao, M., ... coauthors (2011). The dynamical core, physical parameterizations, and basic simulation characteristics of the atmospheric component AM3 of the GFDL Global Coupled Model CM3. *J. Clim.*, *24*, 3484-3519.
- Eyring, V., Bondy, S., Meehl, G. A., Senior, C. A., Stevens, B., Stouffer, R. J., &

- Taylor, K. E. (2016). Overview of the Coupled Model Intercomparison Project phase 6 (cmip6) experimental design and organization. *Geosci. Model Dev.*, 9, 1937-1958. doi: 10.5194/gmd-9-1937-2016
- Fan, S., Ginoux, P., Seman, C. J., Silvers, L. G., & Zhao, M. (2019). Toward improved cloud-phase simulation with a mineral dust and temperature-dependent parameterization for ice nucleation in mixed-phase clouds. *J. Atmos. Sci.*, 76, 3655-3667. doi: 10.1175/JAS-D-18-0287.1
- Frierson, D. M. W., Kim, D., Kang, I.-S., Lee, M.-I., & Lin, J. (2011). Structure of AGCM-simulated convectively coupled Kelvin waves and sensitivity to convective parameterization. *J. Atmos. Sci.*, 68, 26-45. doi: 10.1175/2010JAS3356.1
- Gao, Y., Leung, L. R., Zhao, C., & Hagos, S. (2017). Sensitivity of U.S. summer precipitation to model resolution and convective parameterizations across gray zone resolutions. *J. Geophys. Res.*, 122, 2714-2733. doi: 10.1002/2016JD025896
- Gettelman, A., & Morrison, H. (2015). Advanced two-moment bulk microphysics for global models: Part I: off-line tests and comparison with other schemes. *J. Clim.*, 28, 1268-1287. doi: 10.1175/JCLI-D-14-00102.1
- GFDL modeling systems group. (2022). *Fre-nctools (release 2022.02)* [software]. GFDL. Retrieved from <https://github.com/NOAA-GFDL/FRE-NCTools>
- Gill, A. E. (1980). Some simple solutions for heat-induced tropical circulation. *Q. J. Roy. Meteorol. Soc.*, 106, 447-462. doi: 10.1002/qj.49710644905
- Guo, H., Ming, Y., Fan, S., Zhou, L., Harris, L., & Zhao, M. (2021). Two-moment bulk cloud microphysics with prognostic precipitation in GFDL's Atmospheric Model AM4.0: Configuration and performance. *J. Adv. Model. Earth Sy.*, 13. doi: 10.1029/2020MS002453
- Harris, L., Chen, X., Putman, W., Zhou, L., & Chen, J.-H. (2021). *A scientific description of the GFDL finite-volume cubed-sphere dynamical core* (NOAA Technical Memorandum OAR GFDL No. 2021-001). doi: 10.25923/6nhs-5897
- Harris, L., Chen, X., Zhou, L., & Chen, J.-H. (2020). *The nonhydrostatic solver of the GFDL finite-volume cubed-sphere dynamical core* (NOAA Technical Memorandum OAR GFDL No. 2020-003). NOAA OAR GFDL. doi: 10.25923/9wdt-4895
- Harris, L., Zhou, L., Chen, X., & Chen, J.-H. (2020). *The GFDL finite-volume cubed-sphere dynamical core* (NOAA Technical Memorandum No. 2020-001). NOAA OAR GFDL. doi: 10.25923/7h88-c534
- Harris, L., Zhou, L., Kaltenbaugh, A., Clark, S. K., Cheng, K.-Y., & Bretherton, C. S. (2023). A global survey of rotating convective updrafts in the GFDL X-SHIELD 2021 global storm resolving model. *J. Geophys. Res.*, 128. doi: 10.1029/2022JD037823
- Harris, L., Zhou, L., Lin, S.-J., Chen, J.-H., Chen, X., Gao, K., et al. (2020). GFDL SHIELD: a unified system for weather-to-seasonal prediction. *J. Adv. Model. Earth Sy.*, 12. doi: 10.1029/2020MS002223
- Heim, C., Hentgen, L., Ban, N., & Schär, C. (2021). Inter-model variability in convection-resolving simulations of subtropical marine low clouds. *J. Meteorol. Soc. Jpn.*, 99, 1271-1295. doi: 10.2151/jmsj.2021-062
- Herrington, A. R., & Reed, K. A. (2017). An explanation for the sensitivity of the mean state of the Community Atmosphere Model to horizontal resolution on aquaplanets. *J. Clim.*, 30, 4781-4797. doi: 10.1175/JCLI-D-16-0069.1
- Herrington, A. R., & Reed, K. A. (2020). On resolution sensitivity in the Community Atmosphere Model. *Q. J. Roy. Meteorol. Soc.*, 146, 3789-3807. doi: 10.1002/qj.3873
- Houze, R. A. (2004). Mesoscale convective systems. *Rev. Geophys.*, 42. doi: 10.1029/2004RG000150
- Huynh, H. T. (1997). Schemes and constraints for advection. In P. Kutler, J. Flores, & J.-J. Chattot (Eds.), *Fifteenth international conference on numerical*

- methods in fluid dynamics* (p. 498-503). Berlin, Heidelberg: Springer Berlin Heidelberg. doi: 10.1007/BFb0107151
- Jakob, C., & Klein, S. A. (2000). A parameterization of the effects of cloud and precipitation overlap for use in general-circulation models. *Q. J. Roy. Meteorol. Soc.*, *126*, 2525-2544. doi: 10.1002/qj.49712656809
- Jeevanjee, N. (2017). Vertical velocity in the gray zone. *J. Adv. Model. Earth Sy.*, *9*, 2304-2316. doi: 10.1002/2017MS001059
- Jeevanjee, N., & Zhou, L. (2022). On the resolution-dependence of anvil cloud fraction and precipitation efficiency in radiative-convective equilibrium. *J. Adv. Model. Earth Sy.*, *14*. doi: 10.1029/2021MS002759
- Judt, F., Klocke, D., Rios-Berrios, R., Vanniere, B., Ziemer, F., Auger, L., ... Zhou, L. (2021). Tropical cyclones in global storm-resolving models. *J. Meteorol. Soc. Jpn.*, *99*, 576-602. doi: 10.2151/jmsj.2021-029
- Kiladis, G. N., Wheeler, M. C., an K. H. Straub, P. T. H., & Roundy, P. E. (2009). Convectively coupled equatorial waves. *Rev. Geophys.*, *47*, 2008RG000266.
- Lang, T., Naumann, A. K., Stevens, B., & Buehler, S. A. (2021). Tropical free-tropospheric humidity differences and their effect on the clear-sky radiation budget in global storm-resolving models. *J. Adv. Model. Earth Sy.*, *13*. doi: 10.1029/2021MS002514
- Li, F., Collins, W. D., Wehner, M. F., Williamson, D. L., Olson, J. G., & Algieri, C. (2011). Impact of horizontal resolution on simulation of precipitation extremes in an aqua-planet version of Community Atmospheric Model (CAM3). *Tellus A*, *63*, 884-892. doi: 10.1111/j.1600-0870.2011.00544.x
- Lin, P., Ming, Y., & Robinson, T. (2023). *Dataset supporting "on the resolution sensitivity of equatorial precipitation in a gfdl global atmospheric model" (version 2)* [dataset]. Zenodo. Retrieved from <https://doi.org/10.5281/zenodo.7537434> doi: doi.org/10.5281/zenodo.7537434
- Lin, S.-J. (2004). A "vertically Lagrangian" finite-volume dynamical core for global models. *Mon. Wea. Rev.*, *132*, 2293-2307.
- Lin, S.-J., Zhou, L., Chen, J.-H., Harris, L., Chen, X., & Rees, S. (2018). Evaluation of the FV3-powered next generation unified prediction system for medium-range weather prediction. In *Eighth conference on transition of research to operations*. Austin, Texas. Retrieved from <https://ams.confex.com/ams/98Annual/meetingapp.cgi/Paper/335242>
- Lock, A. P., Brown, A. R., Bush, M. R., Martin, G. M., & Smith, R. N. B. (2000). A new boundary layer mixing scheme. Part I: scheme description and single-column model tests. *Mon. Wea. Rev.*, *128*, 3187-3199.
- Lu, J., Chen, G., Leung, L. R., Burrows, D. A., Yang, Q., Sakaguchi, K., & Hagos, S. (2015). Toward the dynamical convergence on the jet stream in aquaplanet AGCMs. *J. Clim.*, *28*, 6763-6782. doi: 10.1175/JCLI-D-14-00761.1
- Lu, J., Vecchi, G. A., & Reichler, T. (2007). Expansion of the Hadley cell under global warming. *Geophys. Res. Lett.*, *34*. doi: 10.1029/2006GL028443
- Lutsko, N. J., & Cronin, T. W. (2018). Increase in precipitation with surface warming in radiative-convective equilibrium. *J. Adv. Model. Earth Sy.*, *10*, 2992-3010. doi: 10.1029/2018MS001482
- Matsuno, T. (1966). Quasi-geostrophic motions in the equatorial area. *J. Meteorol. Soc. Jpn.*, *44*, 25-43.
- Medeiros, B., Stevens, S., & Bony, S. (2015). Using aquaplanets to understand the robust response of comprehensive climate models to forcing. *Clim. Dyn.*, *44*, 1957-1977. doi: 10.1007/s00382-014-2138-0
- Merlis, T. M., & Held, I. M. (2019). Aquaplanet simulations of tropical cyclones. *Curr. Clim. Change Rep.*, *5*, 185-195. doi: 10.1007/s40641-019-00133-y
- Moncrieff, M. W. (2010). The multiscale organization of moist convection and the intersection of weather and climate. In D.-Z. Sun & F. Bryan (Eds.), *Climate dynamics: Why does climate vary?* (Vol. 189, p. 3-26). Amer. Geophys. Union.

- doi: 10.1029/2008GM000838
- Muller, C. J., & Bony, S. (2015). What favors convective aggregation and why? *Geophys. Res. Lett.*, *42*, 5626-5634. doi: 10.1002/2015GL064260
- Muller, C. J., & Held, I. M. (2012). Detailed investigation of the self-aggregation of convection in cloud-resolving simulations. *J. Atmos. Sci.*, *69*, 2551-2565. doi: 10.1175/JAS-D-11-0257.1
- Neale, R., & Hoskins, B. J. (2000). A standard test for AGCMs including their physical parameterizations: I: the proposal. *Atmos. Sci. Lett.*, *1*, 101-107. doi: 10.1006/asle.2000.0022
- O'Brien, T. A., Collins, W. D., Kashinath, K., Rübel, O., Byna, S., Gu, J., ... Ullrich, P. A. (2016). Resolution dependence of precipitation statistical fidelity in hindcast simulations. *J. Adv. Model. Earth Sy.*, *8*, 976-990. doi: 10.1002/2016MS000671
- O'Gorman, P. A., Li, Z., Boos, W. R., & Yuval, J. (2021). Response of extreme precipitation to uniform surface warming in quasi-global aquaplanet simulations at high resolution. *Phil. Trans. R. Soc. A.*, *379*, 20190543. doi: 10.1098/rsta.2019.0543
- Pendergrass, A. G. (2020). Changing degree of convective organization as a mechanism for dynamic changes in extreme precipitation. *Curr. Clim. Change Rep.*, *6*, 47-54. doi: 10.1007/s40641-020-00157-9
- Rauscher, S. A., O'Brien, T. A., Piani, C., Coppola, E., Giorgi, F., Collins, W. D., & Lawston, P. M. (2016). A multimodel intercomparison of resolution effects on precipitation: simulations and theory. *Clim. Dyn.*, *47*, 2205-2218. doi: 10.1007/s00382-015-2959-5
- Retsch, M. H., Mauritsen, T., & Hohenegger, C. (2019). Climate change feedbacks in aquaplanet experiments with explicit and parameterized convection for horizontal resolutions of 2525 up to 5km. *J. Adv. Model. Earth Sy.*, *11*, 2070-2088. doi: 10.1029/2019MS001677
- Rios-Berrios, R., Medeiros, B., & Bryan, G. H. (2020). Mean climate and tropical rainfall variability in aquaplanet simulations using the Model for Prediction Across Scales-Atmosphere. *J. Adv. Model. Earth Sy.*, *12*. doi: 10.1029/2020MS002102
- Robinson, T., Radhakrishnan, A., & Underwood, S. (2022). *NOAA-GFDL/AM4: Non-hydrostatic aquaplanet MG (version highres-aquaplanet\_2022)* [software]. Zenodo. Retrieved from <https://doi.org/10.5281/zenodo.7476908> doi: 10.5281/zenodo.7476908
- Roh, W., Satoh, M., & Hohenegger, C. (2021). Intercomparison of cloud properties in DYAMOND simulations over the Atlantic Ocean. *J. Meteorol. Soc. Jpn.*, *99*, 1439-1451. doi: 10.2151/jmsj.2021-070
- Rotstaysn, L. D. (1997). A physically based scheme for the treatment of stratiform clouds and precipitation in large-scale models. I: description and evaluation of the microphysical processes. *Q. J. Roy. Meteorol. Soc.*, *123*, 1227-1282. doi: 10.1002/qj.49712354106
- Satoh, M., Stevens, B., Judt, F., Khairoutdinov, M., Lin, S.-J., Putman, W. M., & Düben, P. (2019). Global cloud-resolving models. *Curr. Clim. Change Rep.*, *5*, 172-184. doi: 10.1007/s40641-019-00131-0
- Seo, K.-H., Choi, J.-H., & Han, S.-D. (2012). Factors for the simulation of convectively coupled Kelvin waves. *J. Clim.*, *25*, 3495-3514. doi: 10.1175/JCLI-D-11-00060.1
- Shin, H. H., & Hong, S. (2015). Representation of the subgrid-scale turbulent transport in convective boundary layers at gray-zone resolutions. *Mon. Wea. Rev.*, *143*, 250-271. doi: 10.1175/MWR-D-14-00116.1
- Silvers, L., Blanton, C., McHugh, C., John, J. G., Radhakrishnan, A., Rand, K., ... Zhao, M. (2018). *NOAA-GFDL GFDL-CM4 model output prepared for CMIP6 CFMIP aqua-control*. Earth System Grid Federation. doi:

- 10.22033/ESGF/CMIP6.8512
- Stephan, C. C., Strube, C., Klocke, D., Ern, M., Hoffmann, L., Preusse, P.,  
& Schmidt, H. (2019). Intercomparison of gravity waves in global  
convection-permitting models. *J. Atmos. Sci.*, *76*, 2739-2759. doi:  
10.1175/JAS-D-19-0040.1
- Stevens, B., Satoh, M., Auger, L., Biercamp, J., Bretherton, C. S., Chen, X., ...  
Zhou, L. (2019). DYAMOND: the DYnamics of the Atmospheric general cir-  
culation Modeled On Non-hydrostatic domains. *Prog. Earth Planet Sci.*, *6*, 61.  
doi: 10.1186/s40645-019-0304-z
- Takahashi, Y. O., Hamilton, K., & Ohfuchi, W. (2016). Explicit global simulation of  
the mesoscale spectrum of atmospheric motions. *Geophys. Res. Lett.*, *33*. doi:  
10.1029/2006GL026429
- Terai, C. R., Caldwell, P. M., Klein, S. A., Tang, Q., & Branstetter, M. L. (2018).  
The atmospheric hydrological cycle in the ACME v0.3 model. *Clim. Dyn.*, *50*,  
3251-3279. doi: 10.1007/s00382-017-3803-x
- Tiedtke, M. (1993). Representation of clouds in large-scale models. *Mon. Wea. Rev.*,  
*121*, 3040-3061. doi: 10.1175/1520-0493(1993)121<3040:ROCILS>2.0.CO;2
- Wehner, M. F., Reed, K. A., Li, F., Prabhat, Bacmeister, J., Chen, C.-T., ...  
Jablonski, C. (2014). The effect of horizontal resolution on simulation  
quality in the Community Atmospheric Model, CAM5.1. *J. Adv. Model. Earth  
Sy.*, *6*, 980-997. doi: 10.1002/2013MS000276
- Wheeler, M., & Kiladis, G. N. (1999). Convectively coupled equatorial waves: analy-  
sis of clouds and temperature in the wavenumber-frequency domain. *J. Atmos.  
Sci.*, *56*, 374-399.
- Williamson, D. L., Blackburn, M., Hoskins, B. J., Nakajima, K., Ohfuchi, W., Taka-  
hashi, Y. O., ... Stratton, R. (2012). *The APE atlas* (NCAR Technical note  
Nos. TN-484+STR). NCAR. doi: 10.5065/D6FF3QBR
- Williamson, D. L., Blackburn, M., Nakajima, K., Ohfuchi, W., Takahashi, Y. O.,  
Hayashi, Y.-Y., ... Stratton, R. (2013). The Aqua-Planet Experiment (ape):  
response to changed meridional SST profile. *J. Meteorol. Soc. Jpn.*, *91A*,  
57-89. doi: 10.2151/jmsj.2013-A03
- Williamson, D. L., Kiehl, J. T., & Hack, J. J. (1995). Climate sensitivity of the  
NCAR community climate model (CCM2) to horizontal resolution. *Clim.  
Dyn.*, *11*, 377-397. doi: 10.1007/s003820050082
- Yu, H.-Y., Bao, Q., Zhou, L.-J., Wang, X.-C., & Liu, Y.-M. (2014). Sensitivity of  
precipitation in aqua-planet experiments with an AGCM. *Atmos. Ocean. Lett.*,  
*7*, 1-6. doi: 10.3878/j.issn.1674-2834.13.0033
- Zhang, F., Sun, Y. Q., Magnusson, L., Buizza, R., Lin, S., Chen, J., & Emanuel, K.  
(2019). What is the predictability limit of midlatitude weather? *J. Atmos.  
Sci.*, *76*, 1077-1091. doi: 10.1175/JAS-D-18-0269.1
- Zhang, G., Silvers, L. G., Zhao, M., & Knutson, T. R. (2021). Idealized aquaplanet  
simulations of tropical cyclone activity: significance of temperature gradients,  
Hadley circulations, and zonal asymmetry. *J. Atmos. Sci.*, *78*, 877-902. doi:  
10.1175/JAS-D-20-0079.1
- Zhao, M. (2020). Simulations of atmospheric rivers, their variability, and response to  
global warming using GFDL's new high-resolution general circulation model.  
*J. Clim.*, *33*, 10287-10303. doi: 10.1175/JCLI-D-20-0241.1
- Zhao, M., Golaz, J.-C., Held, I. M., Guo, H., Balaji, V., Benson, R., ... others  
(2018a). The GFDL global atmosphere and land model AM4.0/LM4.0: 1.  
simulation characteristics with prescribed SSTs. *J. Adv. Model. Earth Sy.*, *10*,  
691-734. doi: 10.1002/2017MS001208
- Zhao, M., Golaz, J.-C., Held, I. M., Guo, H., Balaji, V., Benson, R., ... others  
(2018b). The GFDL global atmosphere and land model AM4.0/LM4.0: 2.  
model description, sensitivity studies, and tuning strategies. *J. Adv. Model.  
Earth Sy.*, *10*, 735-769. doi: 10.1002/2017MS001209



- 920 Zhao, M., Held, I. M., & Lin, S.-J. (2012). Some counterintuitive dependencies of  
921 tropical cyclone frequency on parameters in a GCM. *J. Atmos. Sci.*, *69*, 2272-  
922 2283. doi: 10.1175/JAS-D-11-0238.1
- 923 Zhou, L., Lin, S., Chen, J., Harris, L. M., Chen, X., & Rees, S. L. (2019). Toward  
924 convective-scale prediction within the next generation global prediction system.  
925 *Bull. Am. Meteor. Soc.*, *100*, 1225-1243. doi: 10.1175/BAMS-D-17-0246.1